Water Science & Technology

IWA PUBLISHING

Water Science & Technology Vol 89 No 7, 1860 doi: 10.2166/wst.2024.076

Magnetic MoS_2/Fe_3O_4 composite as an effective activator of persulfate for the degradation of tetracycline: performance, activation mechanisms and degradation pathways

Lanhe Zhang[a,†], Qi Zhang[a,†], Tengyue Chen[a], Changyao Wang[a], Chuan Xiao[a], Jingbo Guo[a,*], Xiangrui Pang[b] and Shuhua Liu[c]

[a] School of Chemical Engineering, Northeast Electric Power University, Jilin 132012, China
[b] School of Environment, Liaoning University, Shenyang 110036, China
[c] Jilin Power Supply Company, State Grid Jilin Electric Power Co., Ltd, Jilin 132000, China
*Corresponding author. E-mail: guojingbo640@163.com
†Lanhe Zhang and Qi Zhang are co-first authors.

ABSTRACT

The activated persulfate (PS) process could produce sulfate radical ($SO_4^{\cdot-}$) and rapidly degrade organic pollutants. The application of Fe_3O_4 as a promising PS activator was limited due to the rapid conversion of Fe^{2+} to Fe^{3+} on its surface. Mo^{4+} on MoS_2 surface could be used as a reducing site to convert Fe^{3+} to Fe^{2+}, but the separation and recovery of MoS_2 was complex. In this study, MoS_2/Fe_3O_4 was prepared to accelerate the Fe^{3+}/Fe^{2+} cycle on Fe_3O_4 surface and achieved efficient separation of MoS_2. The results showed that MoS_2/Fe_3O_4 was more effective for PS activation compared to Fe_3O_4 or MoS_2, with a removal efficiency of 91.8% for 20 mg·L^{-1} tetracycline (TC) solution under the optimal conditions. Fe^{2+} and Mo^{4+} on MoS_2/Fe_3O_4 surface acted as active sites for PS activation with the generation of $SO_4^{\cdot-}$, •OH, $\cdot O_2^-$, and $^1O_2$. Mo^{4+} acted as an electron donor to promote the Fe^{3+}/Fe^{2+} cycling and thus improved the PS activation capability of MoS_2/Fe_3O_4. The degradation pathways of TC were inferred as hydroxylation, ketylation of dimethylamino group and C-N bond breaking. This study provided a promising activated persulfate-based advanced oxidation process for the efficient degradation of TC by employing MoS_2/Fe_3O_4 as an effective activator.

Key words: activation, Fe_3O_4, MoS_2, persulfate, tetracycline

HIGHLIGHTS

- MoS_2/Fe_3O_4 was an effective, recoverable PS activator for tetracycline degradation.
- TC was removed by free radical and non-free radical degradation pathways.
- Mo^{4+} promoted the regeneration of Fe^{2+} on the Fe_3O_4 surface.

GRAPHICAL ABSTRACT

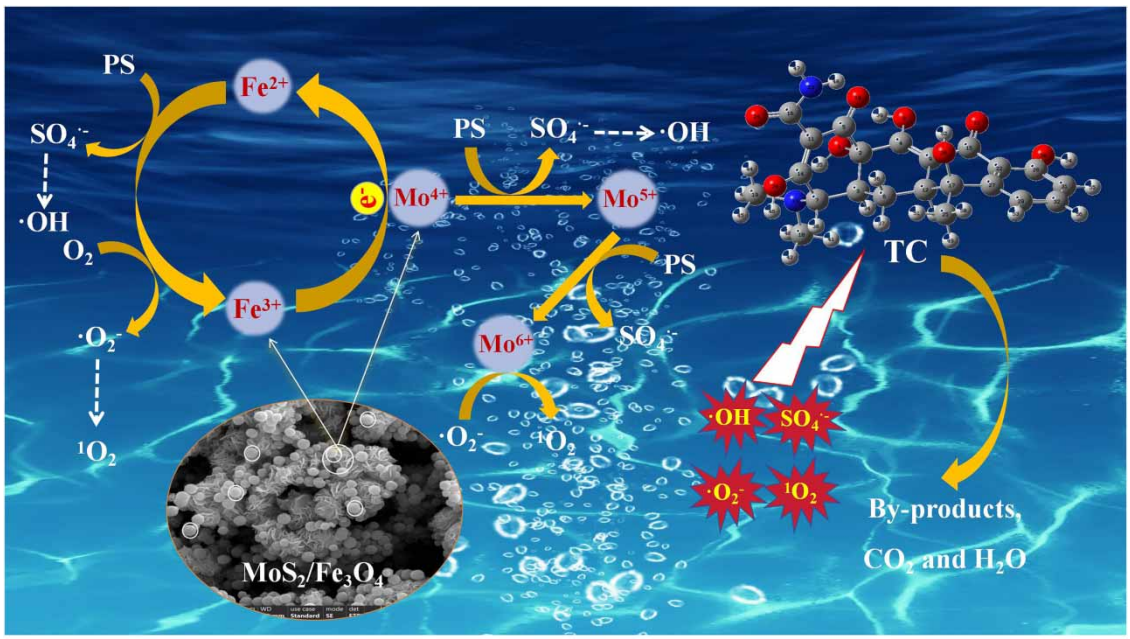

1. INTRODUCTION

Tetracycline (TC), as a broad-spectrum drug, has been widely prescribed for the treatment of bacterial infections in humans and animals (Peng *et al.* 2022). However, only a small portion of TC is absorbed and digested by organisms, while the residue is discharged into the water ecosystem, leading to the occurrence of drug-resistant bacteria and posing a great threat to human health (Cheng & Ji 2022; Liu *et al.* 2022b). Consequently, it is necessary to remove TC from the wastewater (Neolaka *et al.* 2023; Zhang *et al.* 2023d).

Persulfate (PS)-based advanced oxidation processes (AOPs) are considered as an effective method for decomposing pollutants due to their ability to produce sulfate radical ($SO_4^{\bullet-}$) (Wang *et al.* 2023). Compared with hydroxyl ($^{\bullet}OH$), $SO_4^{\bullet-}$ produced by the activated PS has a higher redox potential (2.5–3.1 V) (Zhou *et al.* 2023) and a longer lifetime (30–40 μs) (Wang *et al.* 2022; Shabanloo *et al.* 2023), which is conducive to the degradation and mineralization of the pollutants due to sufficient time provided for $SO_4^{\bullet-}$ diffusion and contact with organic pollutants. $SO_4^{\bullet-}$ can be produced by activating PS using various methods, including ultraviolet (UV), heat, ultrasound, transition metal ions (Diao *et al.* 2020; Du *et al.* 2020; Deng *et al.* 2023; Cabrera-Reina *et al.* 2023) and heterogeneous transition metal catalysts (Cai *et al.* 2022; Zhang *et al.* 2023a). The activation of PS by heterogeneous transition metals is independent of additional energy requirements. Additionally, these metals can be easily recovered after the reaction and thus secondary pollution is avoided, which is more favorable in practical applications (Li *et al.* 2022b, Dai *et al.* 2023).

Recently, Fe_3O_4 was frequently applied to PS activation for the removal of organic pollutants due to its excellent magnetism and environmental friendliness (Peng *et al.* 2018). Fe^{2+} had the ability to activate PS and generate more $SO_4^{\bullet-}$, which was efficient for the degradation of organic pollutants (Zhu *et al.* 2022). Nonetheless, Fe^{2+} on the surface of Fe_3O_4 tended to be oxidized to Fe^{3+} during the activation of PS, and agglomeration was likely to occur among Fe_3O_4 nanoparticles due to their inherent magnetic properties, leading to the reduction of their specific surface area and the efficiency of activating PS (Zhang *et al.* 2022a).

Molybdenum disulfide (MoS_2) was widely utilized in the wastewater treatment due to its low toxicity, abundant active center and high electron mobility (Jlidi *et al.* 2021). It was proved that MoS_2 could be used to activate PS to enhance the degradation of organic pollutants (Wang *et al.* 2021a). Mo^{4+} exposed due to S defect in MoS_2 could be used as an active site to reduce Fe^{3+} to Fe^{2+}, thus promoting the Fe^{3+}/Fe^{2+} recycling (Lu *et al.* 2021). Song *et al.* found that MoS_2 could be used as a cocatalyst of Fe^{2+} to activate PS for the degradation of sulfisoxazole (SIX). The regeneration of Fe^{2+} was accelerated because Mo^{4+} in MoS_2 could convert Fe^{3+} to Fe^{2+}, and the removal efficiency of SIX was as high as 97.1% within 40 min

(Song *et al.* 2020a). Kuang *et al.* added MoS_2 into the Fe^{3+}/PS system to degrade p-chloroaniline (PCA), and the electron-rich Mo^{4+} could transform Fe^{3+} into Fe^{2+} through electron transfer, and thus Fe^{2+} could be continuously produced and continuous degradation of PCA was achieved (Kuang *et al.* 2021). However, the separation and recovery from the solution of MoS_2 could only be performed by repeated filtration or centrifugation, which was a complicated and expensive process.

One possible strategy to solve the above problems is to combine MoS_2 and Fe_3O_4 to prepare a magnetic MoS_2/Fe_3O_4 composite, which can realize rapid separation and recovery of MoS_2 under a magnetic field. Mo^{4+} in MoS_2 can promote the Fe^{3+}/Fe^{2+} cycle on the surface of Fe_3O_4 and improve its catalytic activity. However, there are few reports on MoS_2/Fe_3O_4 as a PS activator, and the mechanisms are still unclear.

In this study, MoS_2/Fe_3O_4 was prepared as a PS activator by solvothermal hydrothermal method for the effective removal of TC. The structure, morphology and chemical composition of MoS_2/Fe_3O_4 were explored and its catalytic performance for PS was evaluated. Meanwhile, the effects of MoS_2/Fe_3O_4 dosage, PS concentration, initial pH, temperature and common inorganic anions on TC degradation were investigated. The mechanisms of MoS_2/Fe_3O_4 as a PS activator were proposed, the possible degradation pathways of TC in the MoS_2/Fe_3O_4/PS system were revealed, and the risk of TC and its degradation intermediates to aquatic organism were predicted. It is anticipated that MoS_2/Fe_3O_4 can serve as an efficient PS activator for the enhanced degradation of TC and simultaneously be separated and recovered by simple operations.

2. MATERIALS AND METHODS

2.1. Chemicals

Detailed information on chemicals and reagents was shown in the Supporting Materials (Text S1).

2.2. Synthesis of catalysts

2.2.1. Synthesis of Fe_3O_4

Fe_3O_4 was prepared using a solvothermal method (Dolatabadi *et al.* 2023). Specifically, 1.2 g $FeCl_3{\cdot}6H_2O$ and 0.5 g $Na_3C_6H_5O_7{\cdot}2H_2O$ were dissolved in 30 mL ethylene glycol (EG) solution at 35 °C by magnetic stirring. Then 3.04 g CH_3COONa was added into the above solution and stirred for 1 h to obtain the precursor. The precursor was poured into a 50 mL Teflon-lined stainless steel autoclave and placed in a constant temperature oven at 200 °C for 12 h. The resulting solid products were collected, washed alternately with deionized water and anhydrous ethanol and then dried in a vacuum drying oven at 55 °C for 10 h to obtain Fe_3O_4 nanoparticles.

2.2.2. Synthesis of MoS_2/Fe_3O_4

First, 1 mmoL of $(NH_4)_6Mo_7O_{24}{\cdot}4H_2O$ was added to 35 mL deionized water by stirring. Different doses of Fe_3O_4 (0.1, 0.15 and 0.2 g) were added and stirred for 30 min. Then, 2.66 g thiourea was added to the above mixture and stirred again for 30 min. The mixture was then transferred into a 50 mL Teflon-lined stainless steel autoclave and placed in a constant temperature oven at 180 °C for 12 h. Then the solid products were collected and washed alternately with deionized water and anhydrous ethanol. After drying at 55 °C for 10 h in a vacuum drying oven, MoS_2/Fe_3O_4 was obtained, which was labeled as FeM-0.1, FeM-0.15, and FeM-0.2 based on the dosage of Fe_3O_4, respectively.

2.3. Characterization

Detailed information on characterization was given in the Supporting Materials (Text S2).

2.4. Experimental procedure

400 mL TC (20 $mg{\cdot}L^{-1}$) was added into a 500 mL beaker and placed in a thermostatic water bath (25 °C) for magnetic agitation. The initial pH of the solution was adjusted using 0.1 $mol{\cdot}L^{-1}$ HCl or 0.1 $mol{\cdot}L^{-1}$ NaOH, and then 4 $mmol{\cdot}L^{-1}$ PS and 0.4 $g{\cdot}L^{-1}$ MoS_2/Fe_3O_4 were added to initiate the reaction. At an interval of 10 min, a 5 mL aliquot sample was collected and filtered by a 0.22 μm filter. At the same time, the reaction was immediately terminated with 0.5 mL $Na_2S_2O_3$ (0.1 $mol{\cdot}L^{-1}$). After the reaction, MoS_2/Fe_3O_4 was recovered and washed alternately with deionized water and anhydrous ethanol three times. Finally, it was dried under vacuum conditions at 60 °C for the recycling experiment.

2.5. Analysis methods

TC concentration was detected using a UV-visible spectrophotometer (UV-1800, AUCY Scientific, China) at 357 nm (Fatimah *et al.* 2023). The pH meter (Five Easy Plus, Mettler-Toledo, China) was used to determine the pH of the solution. The

inductively coupled plasma spectrometry (ICP, Agilent 700 ICP-OES, USA) was used to detect the concentrations of the leaching metal ions in the liquid in the reaction system. Electron paramagnetic resonance spectroscopy (EPR, Bruker A300, Germany) was used to analyze the active species for TC degradation. The degradation intermediates of TC were identified using a liquid chromatography-mass spectrometer (LC-MS, Waters 2695, USA) and the details are shown in Text S3. The calculation method and data for the Fukui function are presented in Text S4. Details of the degradation intermediates and their toxicity assessment are summarized in Text S5 and Table S3.

2.6. Effect of loading dose of Fe_3O_4 in MoS_2/Fe_3O_4 on TC degradation

As presented in Fig. S1, the degradation efficiency of TC was 91.8% in the MoS_2/Fe_3O_4 system, while it decreased to 85.5 and 81.1% in the FeM-0.1 and FeM-0.2 systems, respectively. It was reported that the specific surface area and the number of active sites increased with the rising addition of Fe_3O_4, consequently improving the TC degradation efficiency (Li *et al.* 2023e; Sun *et al.* 2020). However, excessive Fe_3O_4 might cover the reactive active site on the MoS_2 surface and influence the electron transfer (Song *et al.* 2023). As a result, FeM-0.15 was chosen for further investigation, and MoS_2/Fe_3O_4 was referred to FeM-0.15 in the following discussion.

3. RESULTS AND DISCUSSION

3.1. Characterization of MoS_2/Fe_3O_4

As shown in Figure 1, the peaks located at 18.31°, 30.12°, 35.48°, 43.12°, 57.03° and 62.62° corresponded to (111), (220), (311), (400), (511) and (440) planes of Fe_3O_4 (PDF#75-0033), respectively. The detected diffraction peaks at 14.38°, 32.68°, 33.51°, 39.54°, 49.79°, 58.33° and 60.14° matched with the (002), (100), (101), (103), (105), (110) and (008) crystal planes of MoS_2 (PDF#37-1492), respectively. MoS_2/Fe_3O_4 presented the characteristic peaks of MoS_2 and Fe_3O_4. The absence of individual peaks could be attributed to the low crystallinity of MoS_2/Fe_3O_4 (Lu *et al.* 2021), which demonstrated MoS_2/Fe_3O_4 was successfully synthesized using a precipitation-hydrothermal method.

Figure 2(a) shows that Fe_3O_4 appeared as uniform spherical nanoparticles with an approximate diameter of 100 nm. In Figure 2(b), MoS_2 presented a flower-like microsphere structure assembled from nanosheets of different dimensions, and its average diameter was about 5 μm. Figure 2(c) shows that Fe_3O_4 nanoparticles were uniformly attached on the surface of MoS_2 to form MoS_2/Fe_3O_4, which could effectively avoid the agglomeration of Fe_3O_4 nanoparticles. As present in Figure 2(d), the MoS_2 nanofakes and Fe_3O_4 nanoparticles were observed, and Fe_3O_4 nanoparticles were embedded into the nanofakes of MoS_2. Figure 2(e) displays that two distinct lattice fringes were observed in the HRTEM image of MoS_2/Fe_3O_4. The fringes with lattice spacing of 0.210 and 0.274 nm corresponded to the (400) planes of Fe_3O_4 and (100) planes of MoS_2, respectively (Yi *et al.* 2021; Yu *et al.* 2022).

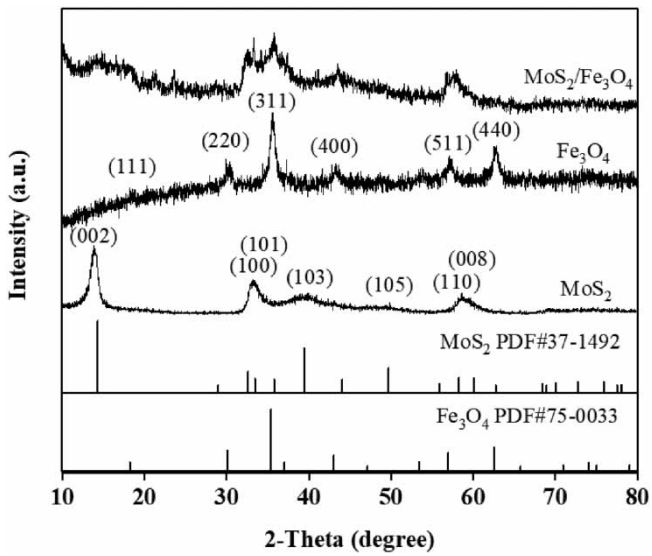

Figure 1 | XRD pattern of MoS_2/Fe_3O_4.

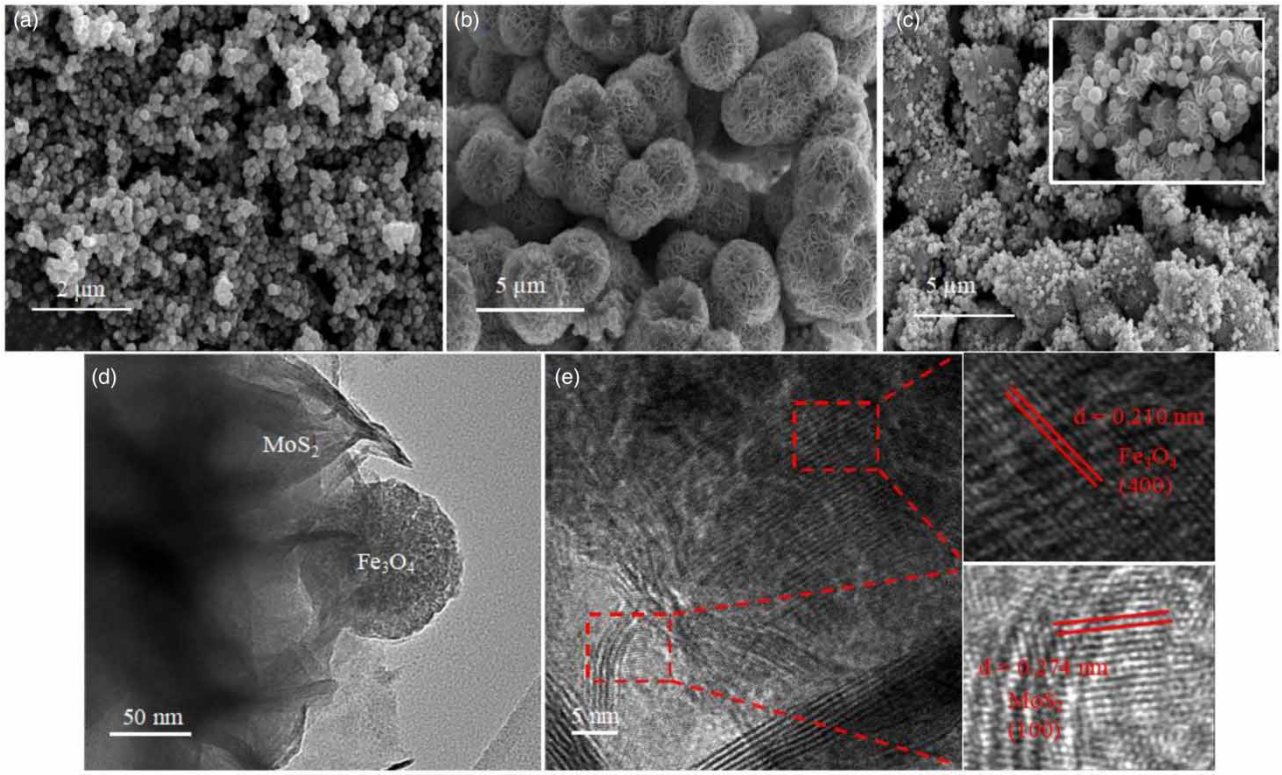

Figure 2 | (a) SEM image of Fe_3O_4; (b) SEM image of MoS_2; (c) SEM image of MoS_2/Fe_3O_4; (d) TEM image of MoS_2/Fe_3O_4; (e) HRTEM image of MoS_2/Fe_3O_4.

As shown in Figure 3(a), only Mo, S, Fe and O elements were observed on the surface of MoS_2/Fe_3O_4, with an atomic ratio of Fe/Mo of 1:1.5. EDS element mapping (Figure 3(b)–3(f)) revealed that Mo, S, Fe and O elements were uniformly distributed, further affirming that Fe_3O_4 were successfully anchored on MoS_2 and thus achieved favorable PS activation. Additionally, Guo *et al.* (2023) also demonstrated that better dispersity provided more active sites on the surface of the composite, contributing to the synergistic effect between MoS_2 and Fe_3O_4 and PS activation.

As shown in Figure 4(a), the peaks detected at 710.6 and 724.3 eV corresponded to Fe^{2+} $2p_{3/2}$ and Fe^{2+} $2p_{1/2}$, respectively, while the peaks at 713.1 and 727.1 eV were attributed to Fe^{3+} $2p_{3/2}$ and Fe^{3+} $2p_{1/2}$, respectively. The peaks located at 719.1 and 733.3 eV were satellite peaks of Fe $2p_{3/2}$ and Fe $2p_{1/2}$, respectively (Huang *et al.* 2019; Tong *et al.* 2022). The two typical peaks at 228.5 and 231.8 eV in Figure 4(b) were assigned to Mo^{4+} $3d_{5/2}$ and Mo^{4+} $3d_{3/2}$, respectively (Li *et al.* 2022c). A weak peak at 235.3 eV was ascribed to Mo^{6+} because negligible MoS_2 was oxidized into MoO_3. The peaks at 229.5 and 232.80 eV corresponded to Mo^{5+} $3d_{5/2}$ and Mo^{5+} $3d_{3/2}$ of MoS_2. A peak detected at 225.6 eV was attributed to S 2s of MoS_2. In the O 1s spectra of MoS_2/Fe_3O_4 (Figure 4(c)), two peaks located at 530.2 and 531.7 were defined as the lattice oxygen in metal oxides (M-O) and surface hydroxyl group (-OH), respectively (Huang *et al.* 2019). For the S 2p spectra of MoS_2/Fe_3O_4 (Figure 4(d)), the peaks at 161.4 and 162.7 eV were assigned to S $2p_{3/2}$ and S $2p_{1/2}$, respectively (Luo *et al.* 2021a). Based on the above characteristics, MoS_2/Fe_3O_4 had been successfully synthesized.

The recovery of the magnetic compounds was simple, which could reduce the operating costs and the secondary pollution (Fernández-Velayos *et al.* 2022; Swami *et al.* 2023). As shown in Figure 5, MoS_2/Fe_3O_4 exhibited superparamagnetism with a saturation magnetization of 9.73 emu g^{-1}. In addition, MoS_2/Fe_3O_4 could be separated from the solution within 120 s under the action of the magnet as shown in Figure 5, avoiding its unnecessary loss (Wang *et al.* 2021b).

3.2. TC degradation

3.2.1. PS activation performance of MoS_2/Fe_3O_4

As shown in Figure 6(a), only 6.1% of TC could be removed within 60 min in a single PS system, while 15.2% when MoS_2/Fe_3O_4 was used due to the limited adsorption of TC by MoS_2/Fe_3O_4. The removal efficiencies of TC in the Fe_3O_4/PS and

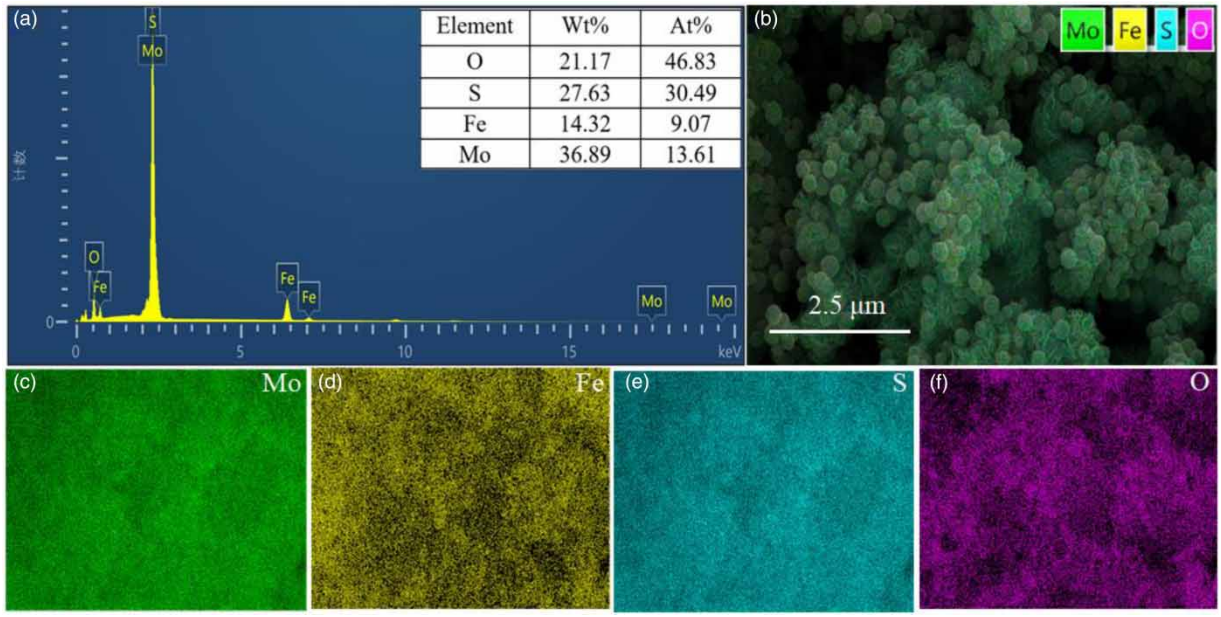

Figure 3 | (a) EDS pattern of MoS_2/Fe_3O_4; (b–f) EDS element mapping of Mo, Fe, O and S of MoS_2/Fe_3O_4.

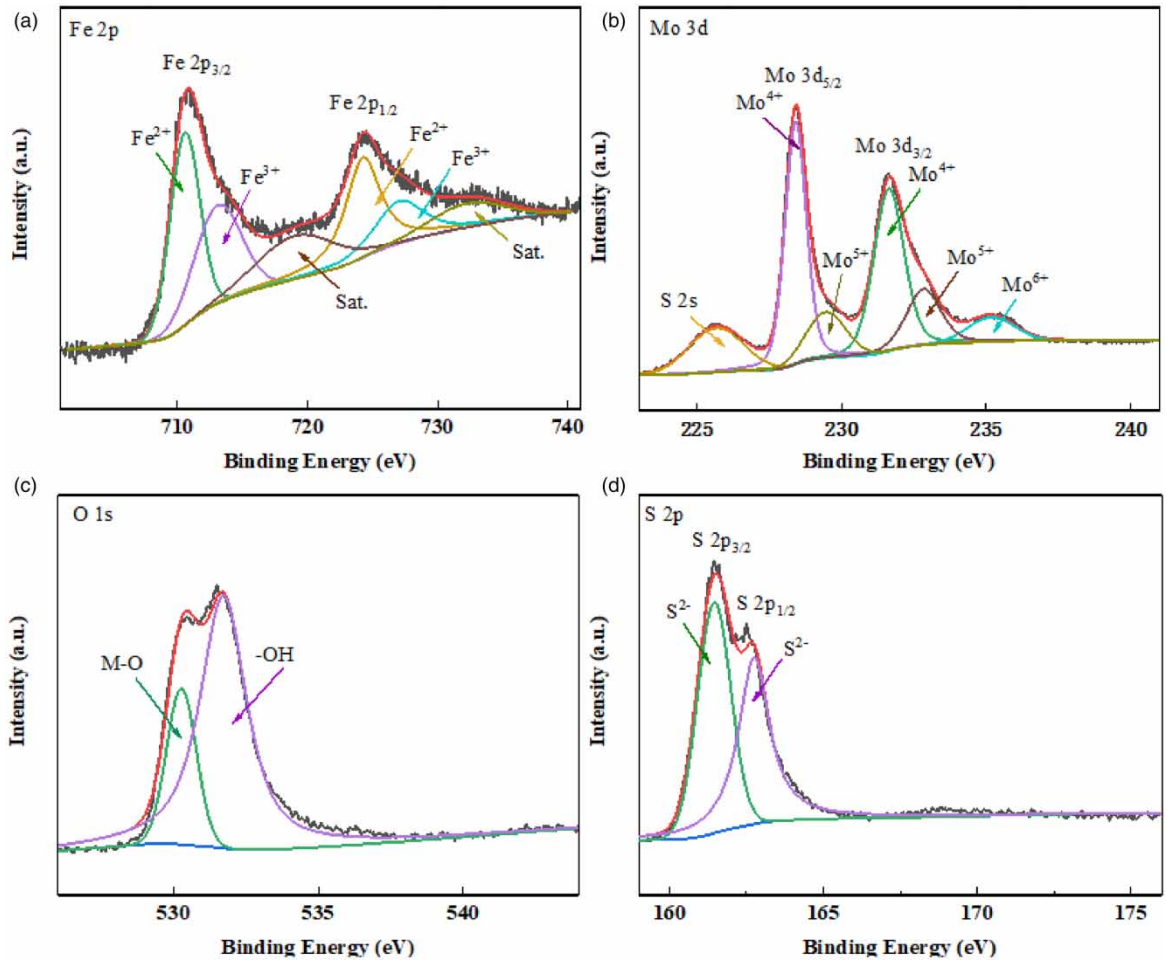

Figure 4 | XPS spectra of the MoS_2/Fe_3O_4: (a) Fe 2p, (b) Mo 3d, (c) O 1s and (d) S 2p.

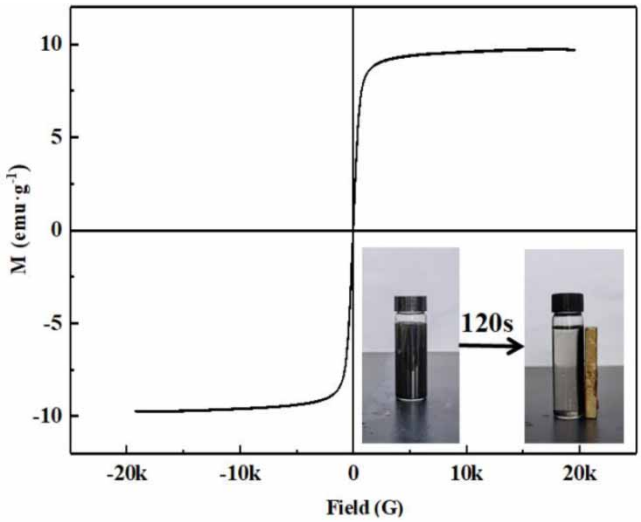

Figure 5 | *M–H* curve of MoS_2/Fe_3O_4.

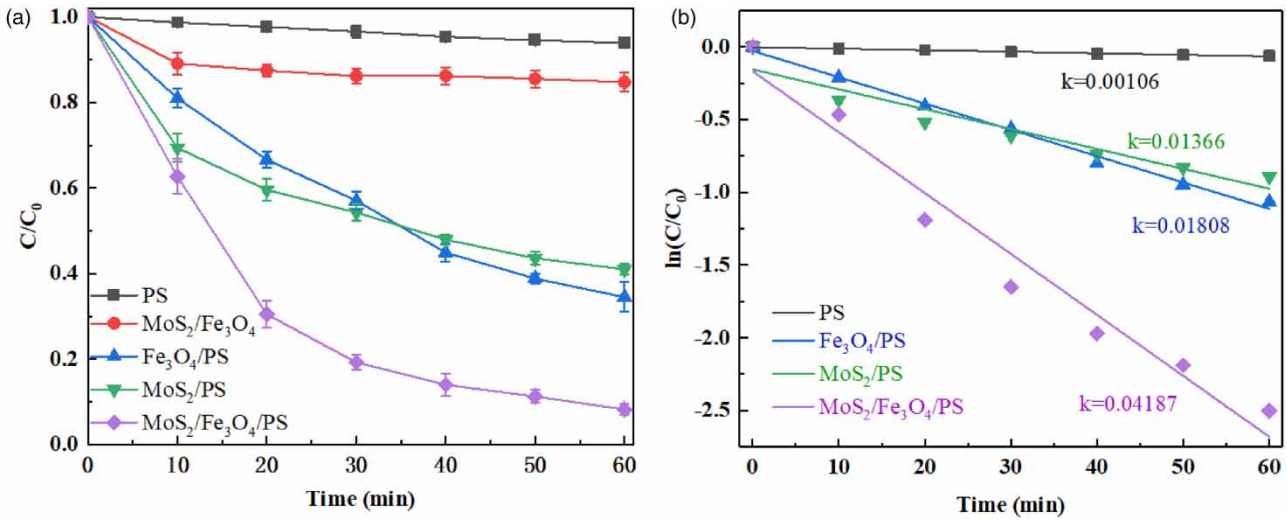

Figure 6 | (a) Removal efficiency of TC in various systems. (b) Kinetics of TC degradation. Reaction conditions: $[MoS_2/Fe_3O_4] = 0.4\ g{\cdot}L^{-1}$, [PS] = 4 mmoL, [TC] = 20 $mg{\cdot}L^{-1}$, initial pH = 7, $T = 25$ °C and reaction time = 60 min.

MoS_2/PS systems were 65.5 and 59%, respectively. These results showed that a single Fe_3O_4 or single MoS_2 was invalid in activating PS to degrade TC. However, in the MoS_2/Fe_3O_4/PS system, the removal efficiency of TC was significantly improved to 91.8% after 60 min reaction, which was much higher than the Fe_3O_4/PS or MoS_2/PS systems as there might be a synergistic effect between MoS_2 and Fe_3O_4 for PS activation. The degradation of TC followed the first-order reaction kinetic model ($R^2 > 0.92$), as shown in Figure 6(b). The reaction rate constant (k_{obs}) values for PS, Fe_3O_4/PS, MoS_2/PS and MoS_2/Fe_3O_4/PS systems were 0.00106, 0.01808, 0.01366 and 0.04187 min^{-1}, respectively. The k_{obs} values of the MoS_2/Fe_3O_4/PS system were 39.5, 2.32 and 3.06 times higher than those of PS, Fe_3O_4/PS and MoS_2/PS systems, respectively. As shown in Table 1, compared with similar studies, we used the hydrothermal method to load Fe_3O_4 nanoparticles onto MoS_2 of flower-shaped microspheres, avoiding the aggregation of Fe_3O_4 nanoparticles and accelerating the surface Fe^{3+}/Fe^{2+} cycling. The preparation method was simple and a small amount of MoS_2/Fe_3O_4 could effectively degrade TC in a short time. In summary, MoS_2/Fe_3O_4 exhibited efficient catalytic ability for TC degradation.

Table 1 | Comparison of this work with previous reports on the use of different catalysts to degrade TC

Catalyst	Preparation method	Structure	Dosage ($g \cdot L^{-1}$)	TC ($mg \cdot L^{-1}$)	Reaction time (min)	Removal efficiency (%)	Reference
Fe_3O_4	Commercial purchase	Nanoparticles	1	100	90	89.0	Hou *et al.* (2012))
Fe_3O_4@JDC	Soaking and calcination method	Nanoparticles anchored on the surface of tubular JDC	0.1	10	60	90.2	Zhang *et al.* (2023c)
BC300-MoS_2-1	Hydrothermal method	Flower-like cluster framework	0.05	20	120	78	Su *et al.* (2022)
FeOOH@MoS_2	Hydrothermal-chemical deposition method	Nanosheet structure	0.4	50	30	85	Yi *et al.* (2021)
Fe_3O_4/CoS_2	Hydrothermal method	Regular polyhedron	0.1	20	20	88.3	Qiu *et al.* (2024)
C@Fe_3O_4	One-pot hydrothermal method	Hollow sphere structure	0.5	100	90	78.5	Peng *et al.* (2018)
$CoFe_2O_4$@MoS_2	One-pot hydrothermal method	Nanoparticles distributed in the MoS_2 flakes	0.2	10	30	80.4	Peng *et al.* (2022)
Fe_3O_4/MoS_2	Hydrothermal method	Nanoparticles attached on the surface of MoS_2	0.4	20	60	91.8	This work

3.2.2. Effects of MoS_2/Fe_3O_4 dosage and PS concentration

As the dosage was increased from 0.1 to 0.4 $g \cdot L^{-1}$, the removal efficiency of TC improved from 61.3 to 91.8% (Figure 7(a)), which could be attributed to the increase of reactive sites for PS activation with higher MoS_2/Fe_3O_4 dosage (Yi *et al.* 2021). However, when the dosage was increased to 0.5 $g \cdot L^{-1}$, the removal efficiency of TC only increased by 1.5%, which suggested that excessive MoS_2/Fe_3O_4 addition could not facilitate TC removal as PS was insufficient. Therefore, 0.5 $g \cdot L^{-1}$ MoS_2/Fe_3O_4 was selected for further experiments.

In Figure 7(b), as the PS concentration was increased from 1.0 to 4.0 $mmol \cdot L^{-1}$, the removal efficiency of TC elevated from 46.3 to 91.8%. When the PS concentration was further increased from 4.0 to 5.0 $mmol \cdot L^{-1}$, the degradation efficiency of TC decreased from 91.8 to 86.9%. It was inferred that the generation rate of free radicals increased with the rising PS concentration, thus enhancing the removal efficiency of TC (Li *et al.* 2023a; Sun *et al.* 2020). However, excessive PS inhibited the degradation of TC because the increased $SO_4^{\bullet -}$ was quenched by itself or PS through the following equations (Li *et al.* 2022c; Liu *et al.* 2022a).

$$SO_4^{\bullet -} + SO_4^{\bullet -} \rightarrow S_2O_8^{2-} \quad (1)$$

$$SO_4^{\bullet -} + S_2O_8^{2-} \rightarrow SO_4^{2-} + S_2O_8^{\bullet -} \quad (2)$$

3.2.3. Effects of pH and temperature

At initial pH values of 3, 5 and 7, the removal efficiencies of TC were 94.8, 93.5 and 91.8%, respectively. However, at initial pH values of 9 and 10, the removal efficiencies of TC decreased to 84.2 and 42.9%, respectively (Figure 7(c)). It was thus inferred that the favorable TC degradation in the MoS_2/Fe_3O_4/PS system could be achieved within the initial pH range of 3–7. The pH in the MoS_2/Fe_3O_4/PS system was monitored during the reaction, as shown in Figure S2. When initial pH values were 3, 5 and 7, the pH dropped below 3.30 after 10 min and continued to decrease in subsequent reactions. When initial pH values were 9 and 10, the pH remained above 3.89 within 60 min. The zero charge point (pH_{PZC}) of the MoS_2/Fe_3O_4 surface was approximately 3.66 (Figure 7(d)). Therefore, the MoS_2/Fe_3O_4 surface carried positive charges after 10 min at initial pH values lower than 7, and $S_2O_8^{2-}$ with negative charges was easily adsorbed on the surface of MoS_2/Fe_3O_4, which promoted the activation of PS and improved the removal efficiency of TC (Zhu *et al.* 2022). However, the MoS_2/Fe_3O_4 surface carried negative charges within 60 min at initial pH values higher than 9, and the electrostatic repulsion prevented the contact between MoS_2/Fe_3O_4 and PS, inhibiting the degradation of TC (Luo *et al.* 2021b).

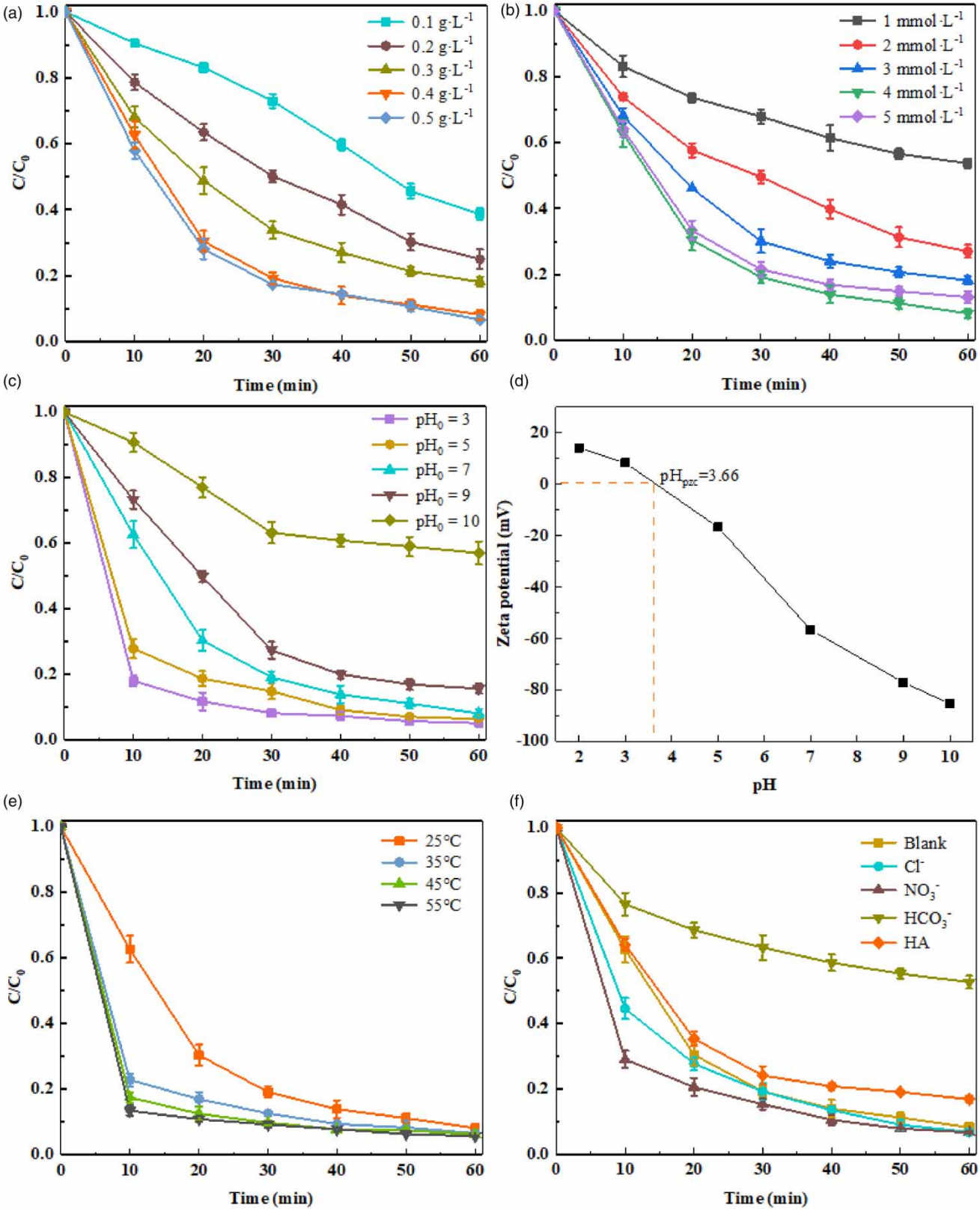

Figure 7 | Effects of reaction parameters on the TC degradation: (a) the dosage of MoS_2/Fe_3O_4; (b) PS concentration; (c) initial pH; (d) Zeta potential of MoS_2/Fe_3O_4 at different pH values; (e) temperature; (f) inorganic anions (Cl^-, NO_3^-, HCO_3^-) and HA. Reaction conditions: [MoS_2/Fe_3O_4] = 0.4 g·L^{-1}, [PS] = 4 mmoL, [TC] = 20 mg·L^{-1}, initial pH = 7, T = 25 °C and reaction time = 60 min.

The effect of temperature on TC degradation in the MoS_2/Fe_3O_4/PS system is shown in Figure 7(e). When the temperature was increased from 25 to 35 °C, the removal efficiencies of TC were higher than 90% after 40 min. When the temperature raised to 45 and 55 °C, the removal efficiency reached 90% after 30 min. It indicated that the elevated temperature could accelerate TC degradation in the MoS_2/Fe_3O_4/PS system. Elevated temperature was conducive to the thermal decomposition of PS, promoting the generation of $SO_4^{\bullet-}$ (Guo *et al.* 2016; Zhang *et al.* 2022b).

3.2.4. Effects of inorganic anions and humic acid

The effects of common inorganic anions (Cl^-, NO_3^- and HCO_3^-) and humic acid (HA) on TC degradation were investigated at a concentration of 3 mmol·L^{-1}. As shown in Figure 7(f), when 3 mmol·L^{-1} Cl^- and NO_3^- were added into the MoS_2/Fe_3O_4/PS system, the removal efficiency of TC increased from 37.5 to 55.4 and 70.1% after 10 min, and from 91.8 to 93.2 and 93.4% after 60 min, respectively, demonstrating that the introduction of Cl^- and NO_3^- accelerated the degradation of TC in the MoS_2/Fe_3O_4/PS system. Cl^- could react with $SO_4^{\bullet-}$ to generate $Cl^{\cdot}$ and $Cl_2^{\bullet-}$, and NO_3^- could be oxidized by $SO_4^{\bullet-}$ to produce $NO_3^{\bullet}$ (Equations (3)–(5)) (Sun *et al.* 2020; Li *et al.* 2023d; Wang *et al.* 2023). Although the oxidation potential of $Cl^{\bullet}$, $Cl_2^{\bullet-}$ and $NO_3^{\bullet}$ was slightly lower than that of $SO_4^{\bullet-}$, they could compensate for the depletion of $SO_4^{\bullet-}$ due to Cl^- and NO_3^- scavenging and enhance the degradation efficiency of TC, which was consistent with previous reports (Song *et al.* 2020a, 2020b). The removal efficiency of TC decreased from 91.8 to 47.3% after 60 min in the presence of HCO_3^-. This was due to the fact that a part of $SO_4^{\bullet-}$ was quenched by HCO_3^- and CO_3^{2-} generated by its ionization (Equations (6) and (7)) (Sun *et al.* 2020; Li *et al.* 2023b). The removal efficiency of TC decreased from 91.8 to 83.2% after adding 3 mmol·L^{-1} HA into the MoS_2/Fe_3O_4/PS system, indicating that HA suppressed TC degradation. Previous studies had shown that HA could act as a free radical quencher by competing with $^{\bullet}OH$ and $SO_4^{\bullet-}$. In addition, the phenolic hydroxyl and carboxyl groups in HA were adsorbed on the surface of MoS_2/Fe_3O_4, blocking the active site and hindering the activation of PS (Li *et al.* 2019).

$$SO_4^{\bullet-} + Cl^- \rightarrow SO_4^{2-} + Cl^{\bullet} \quad (3)$$

$$Cl^{\bullet} + Cl^- \rightarrow Cl_2^{\bullet-} \quad (4)$$

$$SO_4^{\bullet-} + NO_3^{2-} \rightarrow SO_4^{2-} + NO_3^{\bullet} \quad (5)$$

$$SO_4^{\bullet-} + HCO_3^- \rightarrow SO_4^{2-} + HCO_3^{\bullet} \quad (6)$$

$$SO_4^{\bullet-} + CO_3^{2-} \rightarrow SO_4^{2-} + CO_3^{\bullet-} \quad (7)$$

3.3. Mechanisms

3.3.1. EPR testing and quenching experiment

The active species generated in the MoS_2/Fe_3O_4/PS system were identified by EPR testing (Sun *et al.* 2022). As shown in Figure 8(a), no signals were observed in the PS system. In contrast, a DMPO-$^{\cdot}$OH characteristic signal with a peak intensity of 1:2:2:1 was detected in the MoS_2/Fe_3O_4/PS system. This indicated that MoS_2/Fe_3O_4 could effectively activate PS to produce $^{\bullet}OH$. A DMPO – $SO_4^{\bullet-}$ signal formed by DMPO and $SO_4^{\bullet-}$ was also observed in the MoS_2/Fe_3O_4/PS system. The signal intensity of DMPO – $SO_4^{\bullet-}$ was much weaker than that of DMPO-$^{\bullet}OH$, which was attributed to the fact that $SO_4^{\bullet-}$ could react quickly with H_2O to convert into $^{\cdot}OH$ through Equation (8) (Li *et al.* 2022a). In addition, DMPO and TEMP were applied to capture $^{\bullet}O_2^-$ and $^1O_2$. Figure 8(b) and 8(c) showed the characteristic signals of DMPO–$^{\bullet}O_2^-$ and TEMP-$^1O_2$, indicating the generation of $^{\bullet}O_2^-$ and $^1O_2$. The Fe^{2+} on MoS_2/Fe_3O_4 surface could provide an electron for dissolved oxygen to produce $^{\bullet}O_2^-$ (Equation (9)), which was consistent with the research results reported by He *et al.* (2021) and Huang *et al.* (2021). Subsequently, the generated $^{\bullet}O_2^-$ could interact or react with $^{\bullet}OH$ to generate $^1O_2$ (Equations (10) and (11)) (Li *et al.* 2019). Moreover, Mo^{6+} on MoS_2/Fe_3O_4 surface could react with $^{\bullet}O_2^-$ to produce $^1O_2$ (Equation (12)) (Zhang *et al.* 2020). The results of the EPR testing confirmed the presence of $SO_4^{\bullet-}$, $^{\bullet}OH$, $^{\bullet}O_2^-$ and $^1O_2$ in the MoS_2/Fe_3O_4/PS system.

To verify the above conclusions, methanol (MeOH) was used as a quencher for $SO_4^{\bullet-}$ and $^{\bullet}OH$, while tert-butanol (TBA); ascorbic acid (AA); L-histidine (L-H) were used as quenchers for $^{\bullet}OH$, $^{\bullet}O_2^-$ and $^1O_2$, respectively (Li *et al.* 2022c; Peng *et al.* 2022; Liao *et al.* 2011). The removal efficiency of TC decreased from 91.8 to 61.8 and 73.6% with the addition of 1 moL MeOH and TBA, respectively (Figure 8(d)) (Li *et al.* 2022a; Peng *et al.* 2022). The results indicated the presence of $^{\bullet}OH$ and $SO_4^{\bullet-}$ in the MoS_2/Fe_3O_4/PS system, and the contribution of $^{\bullet}OH$ to TC degradation was higher than that of $SO_4^{\bullet-}$. However, MeOH or TBA did not completely inhibit the degradation of TC, indicating the presence of other active species in the

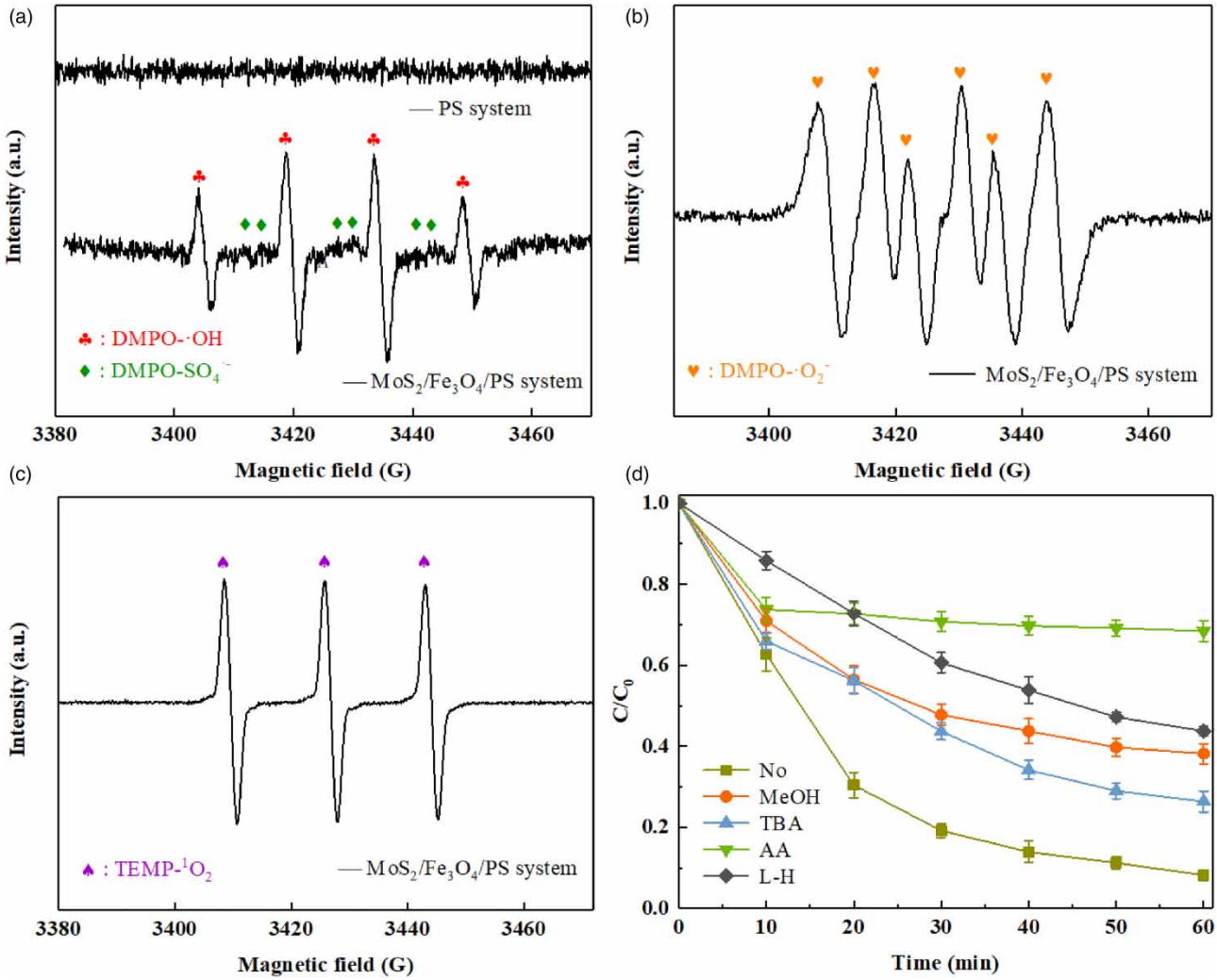

Figure 8 | (a–c) EPR spectrum in the MoS_2/Fe_3O_4/PS system; (d) Effects of radical scavengers on the degradation of TC. Reaction conditions: [MoS_2/Fe_3O_4] = 0.4 g·L^{-1}, [PS] = 4 mmoL, [TC] = 20 mg·L^{-1}, initial pH = 7, T = 25 °C and reaction time = 60 min.

MoS_2/Fe_3O_4/PS system. When 10 mmoL AA and L-H were added into the MoS_2/Fe_3O_4/PS system, the removal efficiency of TC decreased from 91.8 to 31.5 and 56.3%, respectively, confirming that $^{\bullet}O_2^-$ and $^1O_2$ also played an important role in TC degradation (Yang *et al.* 2020, 2022), which was consistent with the EPR test results. According to the results of EPR testing and quenching experiments, $SO_4^{\bullet-}$, $^{\bullet}OH$, $^{\bullet}O_2^-$ and $^1O_2$ were present in the MoS_2/Fe_3O_4/PS system, and $^{\bullet}OH$, $^{\bullet}O_2^-$ and $^1O_2$ were the predominant active species.

$$SO_4^{\bullet-} + H_2O \rightarrow {}^{\bullet}OH + SO_4^{2-} + H^+ \quad (8)$$

$$Fe^{2+} + O_2 \rightarrow Fe^{3+} + {}^{\bullet}O_2^- \quad (9)$$

$$2{}^{\bullet}O_2^- + 2H^+ \rightarrow {}^1O_2 + H_2O_2 \quad (10)$$

$${}^{\bullet}O_2^- + {}^{\bullet}OH \rightarrow {}^1O_2 + OH^- \quad (11)$$

$$Mo^{6+} + {}^{\bullet}O_2^- \rightarrow Mo^{4+} + {}^1O_2 \quad (12)$$

3.3.2. XPS analysis

In order to reveal the mechanism of MoS_2/Fe_3O_4 activating PS, XPS was used to analyze its surface element valence before and after the activation reaction (Figure 9). As shown in Figure 9(a), the proportion of surface Fe^{3+} decreased from 44.7 to 40.4%,

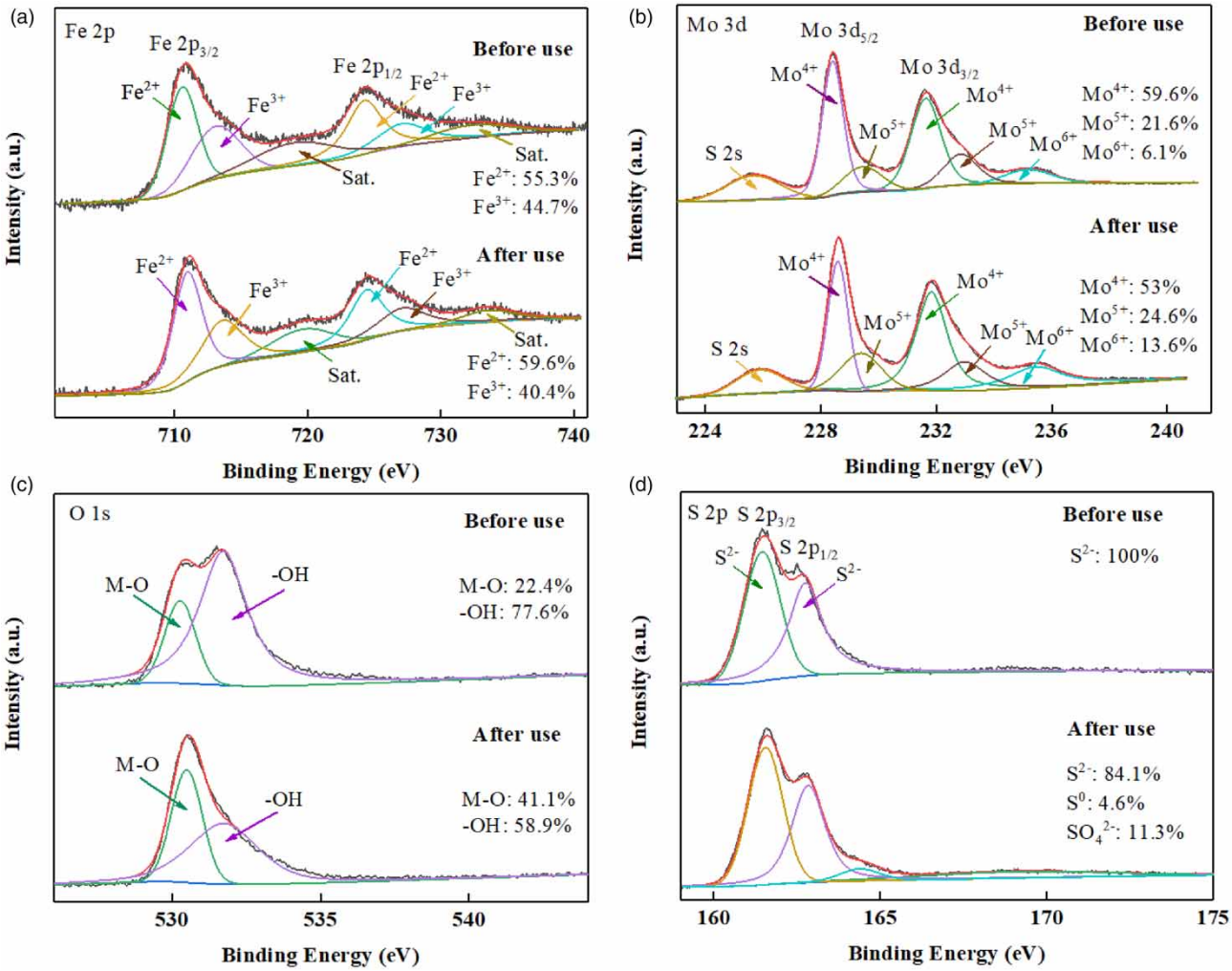

Figure 9 | XPS spectra of MoS_2/Fe_3O_4 before and after use: (a) Mo 3d; (b) Fe 2p; (c) O 1s; (d) S 2p.

while that of Fe^{2+} increased from 55.3 to 59.6% after the activation reaction as a part of Fe^{3+} was reduced to Fe^{2+}. Previous reports had shown that Mo^{4+} contributed to the regeneration of Fe^{2+} and thus accelerated the cycling of Fe^{3+}/Fe^{2+} (Lu *et al.* 2021). Therefore, Fe^{2+} was first oxidized into Fe^{3+} by PS, and then the exposed Mo^{4+} continuously reduced Fe^{3+} to Fe^{2+}, resulting in an increase of Fe^{2+} proportion. The regeneration of Fe^{2+} was a key step in efficient PS activation and the regenerated Fe^{2+} could participate again in the activation of PS and promote the generation of free radicals. As shown in Figure 9(b), the proportion of Mo^{4+} decreased from 59.6 to 53%, and the proportion of Mo^{6+} increased from 6.1 to 13.6%, which demonstrated that a portion of Mo^{4+} was oxidized into Mo^{6+}. As shown in Figure 9(c), the proportion of M-O increased from 22.4 to 41.1% after the reaction, which might be due to the production of molybdenum oxide on the catalyst surface. The proportion of surface -OH decreased from 77.6 to 58.9% after the reaction, indicating that the surface -OH of the catalyst also participated in the reaction. In addition, two new peaks appeared at 163.4 and 169.0 eV after the reaction (Figure 9(d)), indicating the formation of S^0 and $SO_4^{\bullet-}$ on the catalyst surface (Fan *et al.* 2018). This was due to the oxidation of S^{2-} by PS during the reaction process. These results confirmed that Fe_3O_4 and MoS_2 had synergistic effects on PS activation and Mo^{4+} in MoS_2/Fe_3O_4 could reduce Fe^{3+} to Fe^{2+}, promoting the cycling of Fe^{3+}/Fe^{2+} and the production of active species.

3.3.3. Mechanisms of MoS_2/Fe_3O_4 activating PS

Based on the active species identification and XPS analysis, the mechanisms for the PS activation by CuS/Fe_3O_4 were proposed. Firstly, Mo^{4+} and Fe^{2+} on the surface of MoS_2/Fe_3O_4 acted as the active sites to activate PS and produce $SO_4^{\bullet-}$

(Equations (13) and (14)). The generated $SO_4^{\bullet-}$ was further converted to $^{\bullet}OH$ (Equation (15)), and Mo^{4+} and Fe^{2+} were oxidized to Mo^{6+} and Fe^{3+}, respectively. Fe^{2+} on the surface of MoS_2/Fe_3O_4 reacted with dissolved oxygen to form $^{\bullet}O_2^-$, and $^{\bullet}O_2^-$ was further converted to $^1O_2$ by self-reaction or reacting with $^{\cdot}OH$ (Equations (9)–(11)). In addition, Mo^{6+} on MoS_2/Fe_3O_4 surface could react with $^{\bullet}O_2^-$ to produce $^1O_2$ (Equation (12)). Mo^{4+} could be used as an electron donor to reduce Fe^{3+} to Fe^{2+} (Equation (16)). This process promoted the cycle of Fe^{3+}/Fe^{2+} and ensured sufficient Fe^{2+} on the surface of MoS_2/Fe_3O_4 to improve the catalytic activity of MoS_2/Fe_3O_4.

$$Mo^{4+} + S_2O_8^{2-} \rightarrow Mo^{6+} + SO_4^{2-} \quad (13)$$

$$Fe^{2+} + S_2O_8^{2-} \rightarrow Fe^{3+} + SO_4^{\bullet-} + SO_4^{2-} \quad (14)$$

$$SO_4^{\bullet-} + OH^- \rightarrow {}^{\bullet}OH + SO_4^{2-} \quad (15)$$

$$Mo^{4+} + Fe^{3+} \rightarrow Mo^{6+} + Fe^{2+} \quad (16)$$

3.3.4. TC degradation pathway and toxicity assessment

Fukui index was employed to analyze the main sites for reactive species on TC molecule on the basis of the Density functional theory (DFT) calculation (Cheng & Ji 2022; Wu *et al.* 2022). In this study, $SO_4^{\bullet-}$, $^{\bullet}OH$, $^{\bullet}O_2^-$ and $^1O_2$ were the attack species participated in TC degradation in the MoS_2/Fe_3O_4/PS system. Therefore, f^- and f^0 were taken into account to predict the active site of TC in the degradation process (Chen *et al.* 2023). Fukui index (f^0, f^+ and f^-) and the Natural Population Analysis (NPA) charges distribution are shown in Table S1, and the optimized structure of TC is listed in Fig. S3. Generally, the Fukui exponent values with larger f^- and f^0 were more likely to be attacked by $^1O_2$ and free radicals ($SO_4^{\bullet-}$, $^{\cdot}OH$, $^{\bullet}O_2^-$), respectively (Cheng & Ji 2022). Hence, N14 (0.0581) and C7 (0.0751) with higher f^- was susceptible to $^1O_2$ attack. C7 (0.0455) and C12 (0.0401) with larger f^0 values were vulnerable reaction sites for $SO_4^{\bullet-}$, $^{\bullet}OH$, $^{\bullet}O_2^-$ attack, which could undergo oxidation, hydroxylation, and double bond breaking (Zhang *et al.* 2023b). Although C12 had a larger f^0 value, the attack of free radicals was difficult because of the saturated sites and steric hindrance (Wu *et al.* 2023).

According to the detected intermediates (Table S2) and the Fukui index, the possible degradation pathways of TC in the MoS_2/Fe_3O_4/PS system are shown in Figure 10. In path I, C7 was attacked by $SO_4^{\bullet-}$, $^{\cdot}OH$, $^{\bullet}O_2^-$ and $^1O_2$ and TC was

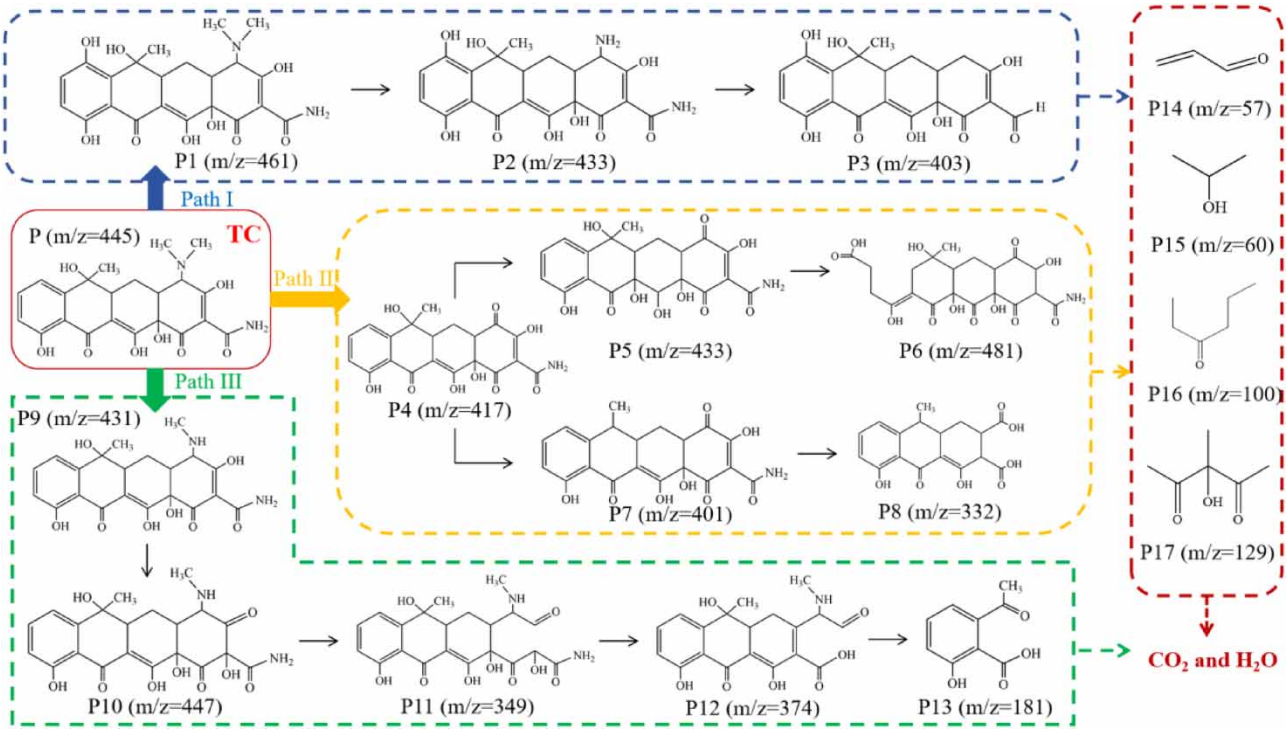

Figure 10 | Degradation pathway of TC.

hydroxylated to produce P1 ($m/z = 461$). P2 ($m/z = 309$) was also formed due to the loss of two dimethyl from P1, and then P2 was converted into P3 ($m/z = 213$) owing to the loss of two amino groups (Wang *et al.* 2017). In path II, N14 tended to be attacked by $^1O_2$ because of its relative larger f^- (0.0581) value. The dimethylamino in the TC was oxidized to the ketone group to form P4 ($m/z = 417$). P4 was hydroxylated to produce P5 ($m/z = 433$). P5 was further oxidized, causing the fracture of the aromatic ring to produce P6 ($m/z = 481$). In addition, P7 ($m/z = 401$) was formed by the dehydration of P4, and P7 was further oxidized by free radicals to form P8 ($m/z = 332$) (Pi *et al.* 2019). In path III, TC was transformed into P9 ($m/z = 431$) owing to the C-N cleavage and dethylation. P10 ($m/z = 447$) was generated owing to the hydroxylation of P9 and could be further oxidized to P11 ($m/z = 349$) by free radicals. P12 ($m/z = 374$) was stemmed from subsequent deamidation of P11 ($m/z = 349$), and was further opened in the ring to produce P13 ($m/z = 181$) (Guo *et al.* 2023). P3, P6, P8 and P13 was further degraded into small organic molecules including P14 ($m/z = 57$), P15 ($m/z = 60$), P16 ($m/z = 100$) and P17 ($m/z = 129$) (Dong *et al.* 2022). Eventually, these short-chain organic molecules were oxidized and decomposed into H_2O and CO_2.

Furthermore, ECOSAR software was applied to predict the toxicity of TC and its intermediate products (Yin *et al.* 2018). The toxicity values for fish LC50 (96 h), daphnid LC50 (48 h) and green algae EC50 (48 h) are presented in Table S3 and the range of toxicity values is shown in Table S4. As demonstrated in Figure 11, the acute toxicity values for fish and green algae were calculated as 61.44 and 17.68 mg·L^{-1}, which was 'harmful'. The value for daphnid was 4.49 mg·L^{-1} in the 'toxic' range. The chronic toxicity value for fish was 0.96 mg·L^{-1}, which was classified as 'very toxic'. The values for daphnid and green algae were 1.04 and 2.52 mg·L^{-1}, which indicated that TC had a certain toxic effect on aquatic organisms. It was worth noting that P3 and P9 were 6.29 and 12.12 mg·L^{-1}, which indicated the slightly higher toxicity to green algae than TC. However, as the oxidation reaction occurred, toxicity values of other intermediates were lower than that of TC, which fell in the 'no harmful' or 'harmful' range, indicating that the MoS_2/Fe_3O_4 system could not only effectively degrade TC, but also reduce certain toxic effects.

3.3.5. Recyclability and stability of MoS_2/Fe_3O_4

As shown in Figure 12(a), after three recycles, the degradation efficiency of TC was still higher than 86% after 60 min, which proved that the MoS_2/Fe_3O_4 had excellent recyclability. The slight decrease of TC degradation efficiency during the recycle experiment might be due to the adsorption of TC degradation intermediates on MoS_2/Fe_3O_4 surface, leading to the plugging of active sites (Sun *et al.* 2020; Li *et al.* 2023c). In addition, the reduction of the proportion of Mo^{4+} on the MoS_2/Fe_3O_4

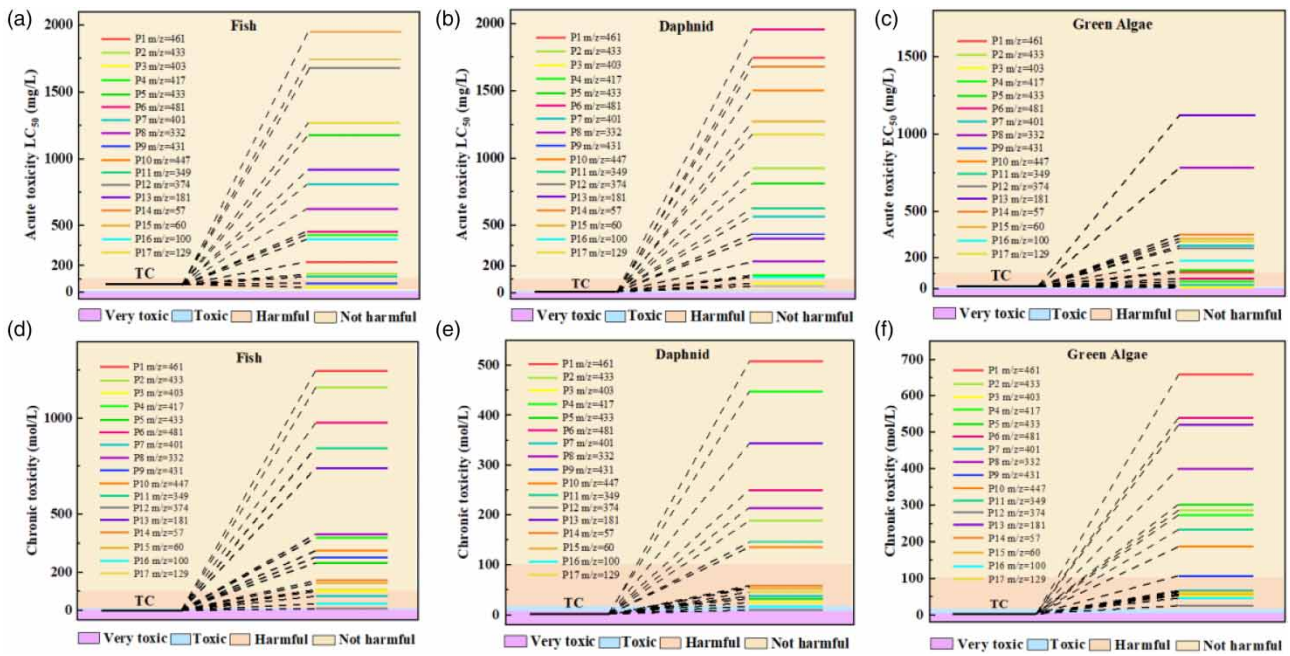

Figure 11 | Acute toxicity of (a) fish LC50 (96 h); (b) daphnid LC50 (48 h); (c) green algae EC50 (48 h); chronic toxicity of (d) fish; (e) daphnid; (f) green algae.

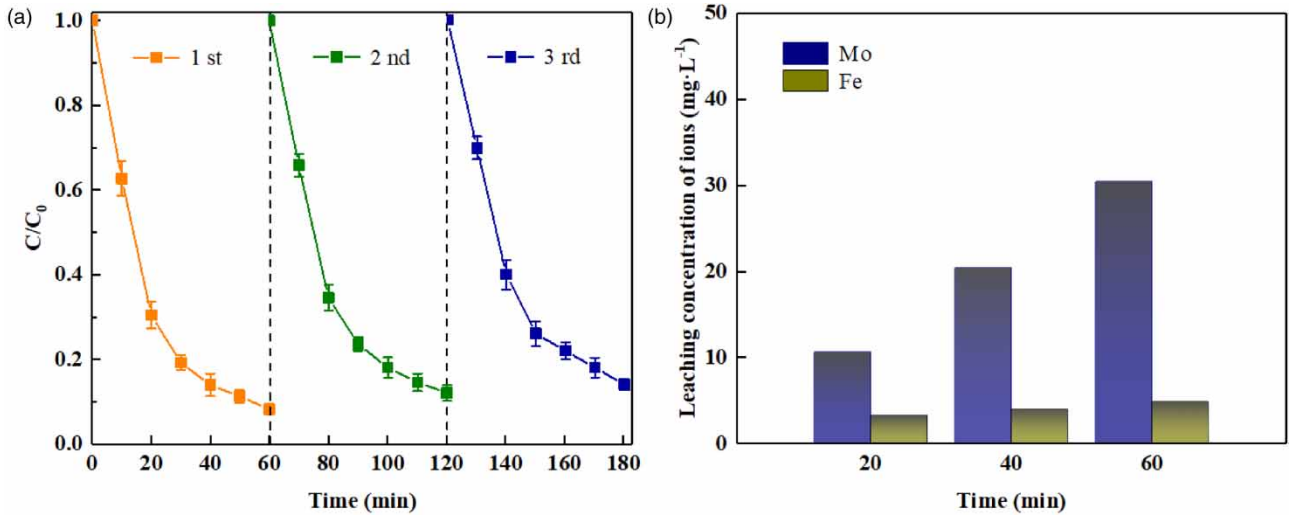

Figure 12 | (a) Recyclability experiments of MoS_2/Fe_3O_4 and (b) leaching concentration of metal ions.

surface during the reaction resulted in the decrease in the conversion efficiency of Fe^{3+} to Fe^{2+}. In order to investigate the stability of MoS_2/Fe_3O_4, the concentration of Mo and Fe ions leached from MoS_2/Fe_3O_4 was monitored by ICP. As shown in Figure 12(b), the concentration of Mo and Fe in the MoS_2/Fe_3O_4/PS system was only 30.4 and 4.85 mg·L^{-1} after 60 min reaction, respectively, which demonstrated its high stability.

4. CONCLUSIONS

In this work, MoS_2/Fe_3O_4 was successfully prepared as PS activator to improve the removal of TC and the separation of MoS_2. Compared to single Fe_3O_4 and MoS_2, MoS_2/Fe_3O_4 had higher activation activity for PS activation, achieving a removal efficiency of 91.8% for 20 mg·L^{-1} TC after 60 min under the conditions of 0.4 g·L^{-1} MoS_2/Fe_3O_4, 4 mmoL PS and pH 7. MoS_2/Fe_3O_4 also demonstrated favorable stability during recycling experiments. The degradation process of TC in the MoS_2/Fe_3O_4 system could be divided into free radical decomposition pathway ($SO_4^{\bullet-}$, $^{\bullet}OH$ and $^{\bullet}O_2^-$) and non-free radical decomposition pathway ($^1O_2$), with $^{\bullet}OH$, $^{\bullet}O_2^-$ and $^1O_2$ identified as the predominant active species. The three major degradation pathways of TC in the MoS_2/Fe_3O_4 system were proposed as hydroxylation, ketylation of dimethylamino group and C-N bond breaking. The toxicity of TC and its intermediates could be effectively reduced by using MoS_2/Fe_3O_4 to activate PS. In conclusion, MoS_2/Fe_3O_4 prepared was an efficient PS activator to promote the decomposition of refractory organic pollutants.

ACKNOWLEDGEMENTS

This work was supported by the Science and Technology Development Program of Jilin Province, China (Nos. 20230203168SF).

AUTHOR CONTRIBUTIONS

L. Z. arranged the resources, wrote the review and edited the article, and rendered support in funding acquisition. Q. Z. investigated the work, rendered support in data curation, and wrote the original draft. T. C. investigated the work and rendered support in data curation. C. W. investigated the work and rendered support in data curation. C. X. investigated the work and edited the article. J. G. supervised the work, arranged the resources, and wrote the review. X. P. investigated the work and edited the article. S. L. validated the article and visualized the data.

DATA AVAILABILITY STATEMENT

All relevant data are included in the paper or its Supplementary Information.

CONFLICT OF INTEREST

The authors declare there is no conflict.

REFERENCES

Cabrera-Reina, A., Aliste, M., Polo-López, M. I., Malato, S. & Oller, I. 2023 Individual and combined effect of ions species and organic matter on the removal of microcontaminants by Fe^{3+}-EDDS/solar-light activated persulfate. *Water Res.* **230**, 119566. https://doi.org/10.1016/j.watres.2023.119566.

Cai, H. T., Chen, M., Li, J., Jin, Y., Ma, Y. J., Ma, Q. & Zhu, P. 2022 Insight into the activation of persulfate with Cu_2O/visible-light: Cu(I) based photo-Fenton and Cu_2O surface mediated free radical mechanism. *Mat. Sci. Semicon. Proc.* **143**, 106502. https://doi.org/10.1016/j.mssp.2022.106502.

Chen, X. J., Yao, L., He, J. H., Li, J. S., Xu, S., Li, N., Zhu, Y. P., Chen, X. & Zhu, R. L. 2023 Enhanced degradation of tetracycline under natural sunlight through the synergistic effect of Ag_3PO_4/MIL-101 (Fe) photocatalysis and Fenton catalysis: Mechanism, pathway, and toxicity assessment. *J. Hazard. Mater.* **449**, 131024. https://doi.org/10.1016/j.jhazmat.2023.131024.

Cheng, L. & Ji, Y. H. 2022 Photocatalytic activation of sulfite by N-doped porous biochar/$MnFe_2O_4$ interface-driven catalyst for efficient degradation of tetracycline. *Green Energy Environ.* https://doi.org/10.1016/j.jwpe.2023.103915.

Dai, X. J., Gu, D. C., Zhou, Q., Zhang, X. F., Zhang, C. Z., Sun, T., Liu, X. Y., Song, D., Gao, L. H., Zheng, J. S., Rao, J. S. & Zhang, Y. X. 2023 Interfacial heterojunction-engineered magnetic Alpha-Fe_2O_3@NiFe LDH@Biotemplate catalyst for heterogeneous photocatalytic activated persulfate removal of organic pollutants. *Colloids Surf. A Physicochem. Eng. Asp.* 132534. https://doi.org/10.1016/j.colsurfa.2023.132534.

Deng, J. Q., Fang, Y., Hou, C. L., Zhang, Y. R., Li, M. F., Han, J. N., Hu, X. J., Du, W. X., Tang, C. F. & Hu, X. J. 2023 Ultrasonic assisted activation of persulfate for the treatment of spent porous biochar: Degradation of adsorbed PFOA and adsorbent regeneration. *J. Environ. Chem. Eng.* 111146. https://doi.org/10.1016/j.jece.2023.111146.

Diao, Z. H., Dong, F. X., Yan, L., Chen, Z. L., Qian, W., Kong, L. J. & Chu, W. 2020 Synergistic oxidation of Bisphenol A in a heterogeneous ultrasound-enhanced sludge biochar catalyst/persulfate process: Reactivity and mechanism. *J. Hazard. Mater.* **384**, 121385. https://doi.org/10.1016/j.jhazmat.2019.121385.

Dolatabadi, M., Świergosz, T., Wang, C. & Ahmadzadeh, S. 2023 Accelerated degradation of groundwater-containing malathion using persulfate activated magnetic Fe_3O_4/graphene oxide nanocomposite for advanced water treatment. *Arab. J. Chem.* **16** (1), 104424. https://doi.org/10.1016/j.arabjc.2022.104424.

Dong, C. Y., Pang, Y., Chen, Y., Gao, Z., Cai, M. Q., Jin, M. C. & Wei, Z. S. 2022 Fe-Ti bimetals catalyst derived from biowaste for highly efficient persulfate activation: Performance and mechanisms. *Process. Saf. Environ. Prot.* **168**, 654–667. https://doi.org/10.1016/j.psep.2022.10.038.

Du, X. Y., Bai, X., Xu, L., Yang, L. & Jin, P. K. 2020 Visible-light activation of persulfate by TiO_2/g-C_3N_4 photocatalyst toward efficient degradation of micropollutants. *Chem. Eng. J.* **384**, 123245. https://doi.org/10.1016/j.cej.2019.123245.

Fan, J. H., Gu, L., Wu, D. L. & Liu, Z. G. 2018 Mackinawite (FeS) activation of persulfate for the degradation of p-chloroaniline: Surface reaction mechanism and sulfur-mediated cycling of iron species. *Chem. Eng. J.* **333**, 657–664. https://doi.org/10.1016/j.cej.2017.09.175.

Fatimah, I., Yanti, I., Putri, F. H. A., Herianto, D., Sagadevan, S., Tamyiz, M. & Doong, R. A. 2023 Phyto-mediated hydrothermal synthesis of $NiFe_2O_4$ as photocatalyst in tetracycline photodegradation. *Environ. Nanotechnol.* **20**, 100879. https://doi.org/10.1016/j.enmm.2023.100879.

Fernández-Velayos, S., Sánchez-Marcos, J., Muñoz-Bonilla, A., Herrasti, P., Menéndez, N. & Mazarío, E. 2022 Direct 3D printing of zero valent iron@polylactic acid catalyst for tetracycline degradation with magnetically inducing active persulfate. *Sci. Total Environ.* **806**, 150917. https://doi.org/10.1016/j.scitotenv.2021.150917.

Guo, H. G., Gao, N. Y., Yang, Y. & Zhang, Y. L. 2016 Kinetics and transformation pathways on oxidation of fluoroquinolones with thermally activated persulfate. *Chem. Eng. J.* **292**, 82–91. http://dx.doi.org/10.1016/j.cej.2016.01.009.

Guo, P. H., Zhou, Y. Q., Zhang, Y. B., Li, Y. K., Lei, H. P., Zhang, H. & Li, S. Q. 2023 Insights into the well-dispersed nano-Fe_3O_4 catalyst supported by N-doped biochar prepared from steel pickling waste liquor for activating peroxydisulfate to degrade tetracycline. *Chem. Eng. J.* **464**, 142548. https://doi.org/10.1016/j.cej.2023.142548.

He, J. J., Wan, Y. & Zhou, W. J. 2021 ZIF-8 derived Fe–N coordination moieties anchored carbon nanocubes for efficient peroxymonosulfate activation via non-radical pathways: Role of FeNx sites. *J. Hazard. Mater.* **405**, 124199. https://doi.org/10.1016/j.jhazmat.2020.124199.

Hou, L., Zhang, H. & Xue, X. 2012 Ultrasound enhanced heterogeneous activation of peroxydisulfate by magnetite catalyst for the degradation of tetracycline in water. *Sep. Purif. Technol.* **84**, 147–152. https://doi.org/10.1016/j.seppur.2011.06.023.

Huang, L., Zeng, T., Xu, X. Y., He, Z. Q., Chen, J. M. & Song, S. 2019 Immobilized hybrids between nitrogen-doped carbon and stainless steel derived Fe_3O_4 used as a heterogeneous activator of persulfate during the treatment of aqueous carbamazepine. *Chem. Eng. J.* **372**, 862–872. https://doi.org/10.1016/j.cej.2019.04.208.

Huang, Q. L., Chen, C. J., Zhao, X. L., Bu, X. Y., Liao, X. F., Fan, H., Gao, X. T., Hu, H. Y., Zhang, Y. J. & Huang, Z. Q. 2021 Malachite green degradation by persulfate activation with $CuFe_2O_4$@biochar composite: Efficiency, stability and mechanism. *Environ. Chem. Eng.* **9**, 105800. https://doi.org/10.1016/j.jece.2021.105800.

Jlidi, Z., Baachaoui, S., Raouafi, N. & Ridene, S. 2021 Temperature effect on structural, morphological and optical properties of 2D-MoS_2 layers: An experimental and theoretical study. *Optik* **228**, 166166. https://doi.org/10.1016/j.ijleo.2020.166166.

Kuang, H. N., He, Z. Y., Li, M., Huang, R. F., Zhang, Y. Q., Xu, X. M., Wang, L., Chen, Y. & Zhao, S. F. 2021 Enhancing co-catalysis of mos_2 for persulfate activation in Fe^{3+}-based advanced oxidation processes via defect engineering. *Chem. Eng. J.* **417**, 127987. https://doi.org/10.1016/j.cej.2020.127987.

Li, X. D., Wu, B., Zhang, Q., Xu, D. P., Liu, Y. Q., Ma, F. J., Gu, Q. B. & Li, F. S. 2019 Mechanisms on the impacts of humic acids on persulfate/Fe^{2+}-based groundwater remediation. *Chem. Eng. J.* **378**, 122142. https://doi.org/10.1016/j.cej.2019.122142.

Li, X. W., Ma, J., Gao, Y. F., Liu, X. T., Wei, Y. & Liang, Z. J. 2022a Enhanced atrazine degradation in the Fe (III)/peroxymonosulfate system via accelerating Fe (II) regeneration by benzoquinone. *Chem. Eng. J.* **427**, 131995. https://doi.org/10.1016/j.cej.2021.131995.

Li, B., Wang, Y. F., Zhang, L. & Xu, H. Y. 2022b Enhancement strategies for efficient activation of persulfate by heterogeneous cobalt-containing catalysts: A review. *Chemosphere* **291**, 132954. https://doi.org/10.1016/j.chemosphere.2021.132954.

Li, X., Zhang, W. W., Liu, Z. X., Wang, S. W., Zhang, X., Xu, B. K. & Sun, Y. J. 2022c Effective removal of tetracycline from water by catalytic peroxymonosulfate oxidation over Co@MoS_2: Catalytic performance and degradation mechanism. *Sep. Purif. Technol.* **294**, 121139. https://doi.org/10.1016/j.seppur.2022.121139

Li, S. Y., Guo, R. X., Li, B. B., Liang, Y. P., Wang, Z. T. & Qu, R. J. 2023a Kinetics and mechanism studies of efficient degradation of 1-hexyl-3-methylimidazolium by zero-valent iron activated persulfate. *Chem. Eng. J.* **460**, 141575. https://doi.org/10.1016/j.cej.2023.141575.

Li, X. D., Shen, J. L., Sun, Z. Q., Zhang, W. W., Ma, F. J. & Gu, Q. B. 2023b Insights into the impacts of chloride ions on the oxidation of 2, 4-dinitrotoluene using ferrous activated persulfate: Removal efficiency, reaction mechanism, transformation pathway, and toxicity assessment. *Chemosphere* **317**, 137887. https://doi.org/10.1016/j.chemosphere.2023.137887.

Li, X., Qin, Y., Song, H. J., Zou, W., Cao, Z. G., Ding, L. J., Pan, Y. W. & Zhou, M. H. 2023c Efficient removal of bisphenol a by a novel biochar-based Fe/C granule via persulfate activation: Performance, mechanism, and toxicity assessment. *Process Saf. Environ. Prot.* **169**, 48–60. https://doi.org/10.1016/j.psep.2022.11.013.

Li, Y. J., Wang, Q. F., Zhang, X., Dong, L., Peng, C., Zhang, M., Yuan, Y. L., Rao, P. H., Gao, N. Y. & Tan, C. Q. 2023d FeOOH@WS_2 as a high-efficiency catalyst for enhanced persulfate activation to remove sulfachloropyridazine. *J. Environ. Chem. Eng.* **11** (6), 111165. https://doi.org/10.1016/j.jece.2023.111165.

Li, Z. L., Zhang, L., Wang, L., Yu, W. G., Zhang, S. X., Li, X. Q. & Zhai, S. R. 2023e Engineering the electronic structure of two-dimensional mos_2 by Ni dopants for pollutant degradation. *Sep. Purif. Technol.* **314**, 123637. https://doi.org/10.1016/j.seppur.2023.123637

Liao, L. W., Yue, H. B. & Cui, Y. D. 2011 Crosslink polymerization kinetics and mechanism of hydrogels composed of acrylic acid and 2-acrylamido-2-methylpropane sulfonic acid. *Chin. J. Chem. Eng.* **19** (2), 285–291. https://doi.org/10.1016/S1004-9541(11) 60167-5.

Liu, H., Huang, C., Wang, P., Huang, S., Yang, X., Xu, H. Y., Zhu, J., Ling, D. X., Feng, C. L. & Liu, Z. M. 2022a A novel Fe/Mo co-catalyzed graphene-based nanocomposite to activate peroxymonosulfate for highly efficient degradation of organic pollutants. *Environ. Res.* **215**, 114233. https://doi.org/10.1016/j.envres.2022.114233.

Liu, L., Han, C. J., Ding, G. F., Yu, M. Y., Li, Y. F., Liu, S. N., Xie, Y. X. & Liu, J. 2022b Oxygen vacancies-enriched Cu/Co bimetallic oxides catalysts for high-efficiency peroxymonosulfate activation to degrade TC: Insight into the increase of Cu^{+} triggered by Co doping. *Chem. Eng. J.* **450** (P3). https://doi.org/10.1016/j.cej.2022.138302.

Lu, J., Zhou, Y. & Zhou, Y. B. 2021 Efficiently activate peroxymonosulfate by Fe_3O_4@ mos_2 for rapid degradation of sulfonamides. *Chem. Eng. J.* **422**, 130126. https://doi.org/10.1016/j.cej.2021.130126.

Luo, N., Chen, C., Yang, D. M., Hu, W. Y. & Dong, F. Q. 2021a S defect-rich ultrathin 2D MoS_2: The role of S point-defects and S stripping-defects in the removal of Cr (VI) via synergistic adsorption and photocatalysis. *Appl. Catal. B.* **299**, 120664. https://doi.org/10.1016/j.apcatb.2021.120664.

Luo, Y. Y., Liu, C., Mehmood, T., Zhang, Y. J., Yu, M. Y. & Ren, Y. Y. 2021b Activation of permonosulfate by Co-Fe_3O_4 composite catalyst for amino acid removal: Performance and mechanism of Co-Fe_3O_4 nanoparticles. *J. Environ. Chem. Eng.* **9** (5), 106036. https://doi.org/10.1016/j.jece.2021.106036.

Neolaka, Y. A., Ngara, Z. S., Lawa, Y., Naat, J. N., Benu, D. P., Chetouani, A., Wang, M. M., Cui, Y. K., Wen, J. T., Wang, Y. S., Jia, M. H., He, S. Z. & Xu, J. 2023 Flexible regulation of persulfate activation mechanisms through tuning Cu valence in CuBTC-derived copper oxide catalysts for improved pollutant degradation. *Chem. Eng. J.* **476**, 146565. https://doi.org/10.1016/j.cej.2023.146565.

Peng, G. L., Zhang, M. H., Deng, S. B., Shan, D. N., He, Q. & Yu, G. 2018 Adsorption and catalytic oxidation of pharmaceuticals by nitrogen-doped reduced graphene oxide/Fe_3O_4 nanocomposite. *Chem. Eng. J.* **341**, 361–370. https://doi.org/10.1016/j.cej.2018.02.064.

Peng, X. M., Yang, Z. H., Hu, F. P., Tan, C. Q., Pan, Q. Y. & Dai, H. L. 2022 Mechanistic investigation of rapid catalytic degradation of tetracycline using $CoFe_2O_4$ @ mos_2 by activation of peroxymonosulfate. *Sep. Purif. Technol.* **287**, 120525. https://doi.org/10.1016/j.seppur.2022.120525.

Pi, Z. J., Li, X. M., Wang, D. B., Xu, Q., Tao, Z. T., Huang, X. D., Yao, F. B., Wu, Y., He, L. & Yang, Q. 2019 Persulfate activation by oxidation biochar supported magnetite particles for tetracycline removal: Performance and degradation pathway. *J. Cleaner Prod.* **235**, 1103–1115. https://doi.org/10.1016/j.jclepro.2019.07.037.

Qiu, F., Pan, Y. N., Wang, L. Y., Song, H. O., Liu, X. Y., Fan, Y. & Zhang, S. P. 2024 Ultrafast degradation of organic pollutants in an Fe_3O_4-CoS_2-x activated persulfate catalytic system with an Fe-Co catalytic cycle involving oxygen and sulfur vacancies. *Sep. Purif. Technol.* **330**, 125139. https://doi.org/10.1016/j.seppur.2023.125139.

Shabanloo, A., Akbari, H., Adibzadeh, A. & Akbari, H. 2023 Synergistic activation of persulfate by ultrasound/pbo$_2$ anodic oxidation system for effective degradation of naproxen, a toxic and bio-recalcitrant pollutant: Process optimization and application for pharmaceutical wastewater. *J. Water Process. Eng.* **54**, 103915. https://doi.org/10.1016/j.jwpe.2023.103915.

Song, X. M., Tian, J. Y., Shi, W. X., Cui, F. Y. & Yuan, Y. X. 2020a Significant acceleration of Fe^{2+}/peroxydisulfate oxidation towards sulfisoxazole by addition of mos$_2$. *Environ. Res.* **188**, 109692. https://doi.org/10.1016/j.envres.2020.109692.

Song, X. L., Ren, C. W., Zhao, Q. Y. & Su, B. Q. 2020b Simultaneous removal of Cr (VI) and triclosan from aqueous solutions through Fe_3O_4 magnetic nanoscale-activated persulfate oxidation. *Chem. Eng. J.* **381**, 122586. https://doi.org/10.1016/j.cej.2019.122586.

Song, X. M., Tian, J. Y., Ma, J. X., Ni, J. X., Liu, D. M., Wang, W., Shi, W. X., Yuan, Y. X., Cui, F. Y. & Chen, Z. W. 2023 Peroxydisulfate activation by a versatile ball-milled nZVI@ mos$_2$ composite: Performance and potential activation mechanism. *Chem. Eng. J.* **453**, 139830. https://doi.org/10.1016/j.cej.2022.139830.

Su, X. Y., Guo, Y. X., Yan, L. G., Wang, Q. D., Zhang, W., Li, X. G., Song, W., Li, Y. F. & Liu, G. C. 2022 Mos$_2$ nanosheets vertically aligned on biochar as a robust peroxymonosulfate activator for removal of tetracycline. *Sep. Purif. Technol.* **282**, 120118. https://doi.org/10.1016/j.seppur.2021.120118.

Sun, H. R., Guo, F., Pan, J. J., Huang, W., Wang, K. & Shi, W. L. 2020 One-pot thermal polymerization route to prepare N-deficient modified g-C_3N_4 for the degradation of tetracycline by the synergistic effect of photocatalysis and persulfate-based advanced oxidation process. *Chem. Eng. J.* **406**, 126844. https://doi.org/10.1016/j.cej.2020.126844.

Sun, X. P., Liu, Z. B. & Sun, Z. R. 2022 Electro-enhanced degradation of atrazine via Co-Fe oxide modified graphite felt composite cathode for persulfate activation. *Chem. Eng. J.* **433**, 133789. https://doi.org/10.1016/j.cej.2021.133789.

Swami, P., Rathod, S., Choudhari, P., Patil, D., Patravale, A., Nalwar, Y. & Hangirgekar, S. 2023 Fe_3O_4@SiO_2@TDI@DES: A novel magnetically separable catalyst for the synthesis of oxindoles. *J. Mol. Struct.* **1292**, 136079. https://doi.org/10.1016/j.molstruc.2023.136079.

Tong, Q., Cai, T., Chen, X. T., Xu, P., Ma, Y. L., Zhao, K. F. & He, D. N. 2022 In-situ reduction-passivation synthesis of magnetic octahedron accumulated by Fe@Fe_3O_4-C core@ complex-shell for the activation of persulfate. *J. Environ. Chem. Eng.* **10** (4), 108116. https://doi.org/10.1016/j.jece.2022.108116.

Yang, J. X., Wang, Z. H., Lv, G. C., Liu, W., Wang, Y., Sun, X. M. & Gao, J. 2020 Indirect photodegradation of fludioxonil by hydroxyl radical and singlet oxygen in aquatic environment: Mechanism, photoproducts formation and eco-toxicity assessment. *Ecotoxicol. Environ. Saf.* **197**, 110644. https://doi.org/10.1016/j.ecoenv.2020.110644.

Yang, Q. X., Yan, Y., Yang, X. F., Liao, G. Y., He, J. & Wang, D. S. 2022 The effect of complexation with metal ions on tetracycline degradation by Fe^{2+}/Fe^{3+} and Ru^{3+} activated peroxymonosulfate. *Chem. Eng. J.* **429**, 132178. https://doi.org/10.1016/j.cej.2021.132178.

Yi, C. H., He, Z. Y., Hu, Y. Z., Liang, D. M., Zhang, Y. Q. & Chen, Y. 2021 FeOOH @ MoS_2 as a highly effective and stable activator of peroxymonosulfate-based advanced oxidation processes for pollutant degradation. *Surf. Interfaces* **27**, 101465. https://doi.org/10.1016/j.surfin.2021.101465.

Yin, K., Deng, L., Luo, J. M., Crittenden, J., Liu, C. B., Wei, Y. F. & Wang, L. L. 2018 Destruction of phenicol antibiotics using the UV/H_2O_2 process: Kinetics, byproducts, toxicity evaluation and trichloromethane formation potential. *Chem. Eng. J.* **351**, 867–877. https://doi.org/10.1016/j.cej.2018.06.164.

Yu, Y. J., Guo, H. B., Zhong, Z. J., Wang, A. Q., Xiang, M. D., Xu, S. H., Dong, C. Y. & Chang, Z. F. 2022 Fe_3O_4 loaded on ball milling biochar enhanced bisphenol a removal by activating persulfate: Performance and activating mechanism. *Environ. Manage.* **319**, 115661. https://doi.org/10.1016/j.jenvman.2022.115661.

Wang, X. N., Jia, J. P. & Wang, Y. L. 2017 Combination of photocatalysis with hydrodynamic cavitation for degradation of tetracycline. *Chem. Eng. J.* **315**, 274–282. https://doi.org/10.1016/j.cej.2017.01.011.

Wang, J. W., Wang, Z. P., Cheng, Y. J., Cao, L. S., Bai, F., Yue, S. Y., Xie, P. C. & Ma, J. 2021a Molybdenum disulfide (MoS_2): A novel activator of peracetic acid for the degradation of sulfonamide antibiotics. *Water Res.* **201**, 117291. https://doi.org/10.1016/j.watres.2021.117291.

Wang, Y., Gao, P. C., Wei, Y. Y., Jin, Y. J., Sun, S., Wang, Z. F. & Jiang, Y. 2021b Silver nanoparticles decorated magnetic polymer composites (Fe_3O_4@PS@Ag) as highly efficient reusable catalyst for the degradation of 4-nitrophenol and organic dyes. *J. Environ. Manage.* **278**, 111473. https://doi.org/10.1016/j.jenvman.2020.111473.

Wang, B. W., Li, X. Y. & Wang, Y. 2022 Degradation of metronidazole in water using dielectric barrier discharge synergistic with sodium persulfate. *Sep. Purif. Technol.* **303**, 122173. https://doi.org/10.1016/j.seppur.2022.122173.

Wang, Q., Zhu, F., Cheng, H., Komarneni, S. & Ma, J. F. 2023 Efficient activation of persulfate by Ti_3C_2 MXene QDs modified $ZnFe_2O_4$ for the rapid degradation of tetracycline. *Chemosphere* **328**, 138546. https://doi.org/10.1016/j.chemosphere.2023.138546.

Wu, K., Tao, C. N., Hu, Z. R., Lei, H., Zhong, J. Y., Li, W., Zhang, C. Q., Wang, M., Yang, S. J. & Liu, T. 2022 Simultaneous removal of tetracycline and arsenic (III) using copper-manganese composite oxide: Competition behaviors and removal mechanisms. *J.Water Process. Eng.* **49**, 103117. https://doi.org/10.1016/j.jwpe.2022.103117.

Wu, W. B., Wang, R. P., Chang, H. X., Zhong, N. B., Zhang, T., Wang, K., Ren, N. Q. & Ho, S. H. 2023 Rational electron tunning of magnetic biochar via N, S co-doping for intense tetracycline degradation: Efficiency improvement and toxicity alleviation. *Chem. Eng. J.* **458**, 141470. https://doi.org/10.1016/j.cej.2023.141470.

Zhang, X., Deng, H., Zhang, G., Yang, F. & Yuan, G. E. 2020 Natural bornite as an efficient and cost-effective persulfate activator for degradation of tetracycline: Performance and mechanism. *Chem. Eng. J.* **381**, 122717. https://doi.org/10.1016/j.cej.2019.122717.

Zhang, H., Mei, Y., Zhu, F., Yu, F., Komarneni, S. & Ma, J. F. 2022a Efficient activation of persulfate by C @ Fe_3O_4 in visible-light for tetracycline degradation. *Chemosphere* **306**, 135635. https://doi.org/10.1016/j.chemosphere.2022.135635.

Zhang, L. B., Wang, Y. Q., Shi, Y. H. & Zhu, Y. H. 2022b Heterogeneous catalytic oxidation of tetracycline hydrochloride based on persulfate activated by Fe_3O_4/MC composite. *Chem. Eng. J.* **447**, 137406. https://doi.org/10.1016/j.cej.2022.137406.

Zhang, L. H., Li, Y. R., Guo, J. B., Kan, Z. F. & Jia, Y. P. 2023a Catalytic ozonation mechanisms of Norfloxacin using Cu-$CuFe_2O_4$. *Environ. Res.* **216**, 114521. https://doi.org/10.1016/j.envres.2022.114521.

Zhang, Q. Z., Tian, J., Hu, Y., Wu, S. L. & Chen, D. Z. 2023b Co@ C core-shell nanostructures anchored on carbon cloth for activation of peroxymonosulfate to degrade tetracycline. *J. Environ. Chem. Eng.* **11** (1), 109197. https://doi.org/10.1016/j.jece.2022.109197.

Zhang, Y. J., Yang, Q., Yue, L. C., Liu, Q., Luo, Y. S., Wu, L. Y., Kang, X. W., Sun, S. J., Yang, Y. C. & Sun, X. P. 2023c Biomass Juncus derived carbon modified with Fe_3O_4 nanoparticles toward activating peroxymonosulfate for efficient degradation of tetracycline. *J. Water Process. Eng.* **51**, 103324. https://doi.org/10.1016/j.jwpe.2022.103324.

Zhang, Y. Q., Liang, B., Ma, X. D., Han, J. L., Li, Z. L., Nie, S. C., Zhang, Z. Y. & Wang, A. J. 2023d Enhancing the anoxic/oxic process for treating hypersaline amide wastewater using a synthetic bacterial agent to regulate core bacterial interactions. *J. Water Process. Eng.* **55**, 104191. https://doi.org/10.1016/j.jwpe.2023.104191.

Zhou, C. S., Cao, G. L., Wu, X. K., Liu, B. F., Qi, Q. Y. & Ma, W. L. 2023 Removal of antibiotic resistant bacteria and genes by nanoscale zero-valent iron activated persulfate: Implication for the contribution of pH decrease. *J. Hazard. Mater.* **452**, 131343. https://doi.org/10.1016/j.jhazmat.2023.131343.

Zhu, L. D., Zhou, Y. X., Fei, L. Y., Cheng, X. L., Zhu, X. X., Deng, L. Q. & Ma, X. 2022 Z-scheme CuO/Fe_3O_4/GO heterojunction photocatalyst: Enhanced photocatalytic performance for elimination of tetracycline. *Chemosphere* **309**, 136721. https://doi.org/10.1016/j.chemosphere.2022.136721.

First received 18 January 2024; accepted in revised form 18 February 2024. Available online 11 March 2024